Response of a Squeeze Film Damper Under High Dynamic Loading and Identification of Damping and Inertia Coefficients

by

Dr. Luis San Andrés

May 2002

TRC-SFD-1-02, May 2002

EXECUTIVE SUMMARY

High performance turbomachinery demands high shaft speeds, increased rotor flexibility, tighter clearances in the flow passages, advanced materials, and increased tolerance to imbalances. Operation at high speeds induces severe dynamic loading with large amplitude journal motions at the bearing supports. At these conditions, oil lubricated dampers and journal bearings with low levels of external pressurization are prone to air ingestion leading to an inhomogeneous lubricant film with large striations of entrapped gas. This pervasive phenomenon affects greatly the dynamic force capability of the support fluid film bearings and reduces the reliability of the rotor-bearing system.

Forced response experiments on a test squeeze film damper for various dynamic load conditions are reported. Shakers exert single frequency loads and induce circular orbits and elliptical orbits of increasing amplitudes. Measurements of the applied loads, bearing displacements and accelerations permit identification of damping and inertia force coefficients for operation at three whirl frequencies (40, 50 and 60 Hz) and increasing lubricant temperatures. Measurements of film pressures reveal an early onset of air ingestion.

Identified damping force coefficients agree well with predictions based on a well-known bearing model if an effective length is used. This length ranges from 82% to 78% of the actual length as the whirl excitation frequency increases. Justifications for the reduced length or effective viscosity follow from the small through flow rate, not large enough to offset the dynamic volume changes. The measurements and analysis thus show the pervasiveness of air entrainment, whose effect increases with the amplitude and frequency of the dynamic journal motions. Identified inertia coefficients are approximately twice as large as those derived from classical theory.

Further experiments are planned to assess the effect of air ingestion in dynamically loaded hydrodynamic bearings, to identify rotordynamic force coefficients, and to advance predictive (semi-empirical) formulae validating the measurements.

TABLE OF CONTENTS

LIST OF TABLES AND FIGURES

Tables

Figures

NOMENCLATURE

a,b	Major and minor amplitudes of elliptical motions [m]
$a_{x,y}$	Bearing housing accelerations [m/s^2]
c	bearing radial clearance [0.127 mm – design]
$C_{sx,sy}$	Dry (no lubricant) damping coefficients [Ns/m]
$C_{\alpha\beta}$	(Estimated) Bearing damping coefficients [N.s/m], $\alpha \beta = X,Y$
C_{tt}	Direct damping coefficient for circular centered orbits [N.s/m]
e	Amplitude of dynamic motion (instantaneous eccentricity) [m]
D	Journal Diameter [0.127 m]
$D_{\alpha\beta}$	(Estimated) Bearing fluid inertia coefficients [N.s^2/m], $\alpha \beta = X,Y$
D_{rr}	Direct inertia coefficient for circular centered orbits [N.s^2/m],
$F_{x,y}$	External (shaker) forces applied to bearing [N]
i	imaginary unit ($\sqrt{-1}$)
$K_{sx,sy}$	Structural (support) stiffnesses [N/m]
L	Bearing length [0.032 m]
L_e	Effective hydrodynamic length for bearing [m]
$l_{(\beta)}$	Length fraction for air entrainment operation [-]
M	Mass of bearing housing [kg]
M_f	Estimated mass of lubricant on housing feed plenum [kg]
Q_Z	Axial (through) flow rate [LPM]
Q_d	$\pi \omega e L D$. Dynamic volume change in squeeze film lands [LPM]
T	Lubricant temperature [°C]
X,Y	Cartesian coordinate system for lateral motions of test bearing
x,y	Bearing dynamic motions along two directions X,Y [m]
r,t	Radial and tangential coordinate system
$\alpha_{(\beta)}$	Effective viscosity fraction due to air entrainment [-]
β	Air entrainment volume fraction within lubricant film [-]
ε	e/c, dimensionless journal (instantaneous) eccentricity
ζ	$C/[2 (K_s M)^{1/2}]$. Viscous damping ratio [-]
γ	(Q_Z/Q_d). Feed – squeeze flow ratio for assessment of air entrainment [-]

ρ Lubricant density [736 kg/m^3]

μ Lubricant viscosity [Pa.s]

ω Excitation frequency [rad/s]

INTRODUCTION

Squeeze Film Dampers (*SFDs*) are effective in reducing vibrations on rotor bearing systems while traversing critical speeds. *SFDs* generate their (damping) force capability in reaction to dynamic journal motions squeezing a thin film of lubricant in the annular region (clearance) between a stationary (bearing) housing and a whirling journal. Dynamic film pressures, characteristic to the type of journal motion, evolve as time-varying fields with magnitudes well above and below the feed and discharge pressures. Lubricant cavitation (vapor or gaseous), and worse yet air ingestion and entrapment within the lubricant film, occurs if the mean film pressure is too low or if the through flow rate is not sufficient to fill the fast volume changes related to the journal kinematics [1,2].

Low feed pressures, large amplitudes of journal motion and operation at high frequencies cause film starvation due to air entrainment (ingestion and entrapment). These operating conditions ultimately affect the bearing forced performance evidencing damping coefficients much lower than predictions based on conventional lubrication models [3,4].

The report presents a test rig for identification of fluid film bearing coefficients from measurements of the dynamic response of the bearing motion due to applied (external) periodic (single frequency) forces exerted by a pair of orthogonally placed shakers. Presently, the bearing operates in a squeeze film damper mode, i.e. without rotor spinning.

The report advances the physical analysis, experimental verification and prediction of forces in a squeeze film damper operating with large orbital motions induced by dynamic loading. This operating condition causes persistent air ingestion and entrapment within the lubricated film lands, affecting greatly the bearing forced response.

1

TEST RIG DESCRIPTION

Figure 1 shows a picture of the test rig and Figure 2 depicts a schematic view of the rig major components and disposition, including the DAQ system. A stiff shaft[1], mounted on three precision ball bearings, holds a steel journal of diameter (D) 127 mm (5") and length (L) 32 mm (1.25"). The bearing housing comprises an acrylic bearing sandwiched by two steel circular plates. The design fluid film bearing radial clearance is 0.127 mm (5 mils). The top plate (cover) includes a connection for lubricant supply through a flexible hose, a static pressure gauge displaying the feed pressure into the bearing, and provisions for installation of four eddy current sensors facing the rotor (shaft). Piezoelectric load cells and accelerometers are attached to small rectangular plates connecting the top and bottom circular plates.

The composite bearing housing hangs from a top structure via four steel rods. These rods provide a structural stiffness to the test bearing section. A mechanism comprising two sliding flat plates on the top structure allows centering or off-centering positioning of the test bearing with respect to the shaft.

Figures 3 and 4 show details of the sensor disposition and reference coordinate system. Two small (maximum 100 N) electromagnetic shakers hang from separate metal structures. Slender steel stingers connect the shaker heads to the bearing housing (x and y directions). Piezoelectric load cells are pre-stressed (in compression) at the ends of the stingers fastened to the side plates on the bearing housing. The side plates also house two piezoelectric accelerometers (x,y).

The acrylic housing permits flow visualization using appropriate stroboscope lighting. This feature is of particular interest for the study of dynamic cavitation or air ingestion in lubricant films. The bearing also contains two type-K thermocouples for measurement of film temperature and two strain-gauge type pressure transducers for measurement of the absolute film pressure. Appendix A lists the sensors' sensitivities used in the present experimental investigation.

Preliminary tests aimed to determine the "dry" system parameters, i.e. without lubricant flowing through the bearing. To this end, static measurements of loads applied

---

[1] The natural frequency of the shaft and journal is ~ 400 Hz, well above the operating speed (maximum 6000 rpm) and excitation frequencies (0-100 Hz).

on the housing and bearing housing displacements (bar deflections) relative to the shaft evidence the structural support stiffness along directions x and y. Figure 5 displays the test results using a (Shimpo) hand held force gauge and displacements recorded from the eddy current sensors. The tests show a linear force versus displacement behavior with nearly identical structural stiffnesses $(K_{sx} \sim K_{sy})$ over a range of displacements to about 100 microns. The natural frequency (f_n) of the bearing-rods support structure in the (x,y) directions is approximately 49-50 Hz. From these values, the simple formula

$$M = K \Big/ (f_n 2\pi)^2$$ renders equivalent masses $(M)_{x,y}$ for the test section. Table 1 shows the

"dry" system parameters, including the viscous damping ratios and damping coefficients. The last parameters, obtained in a prior investigation [5], are derived from impact loads and sine-sweep loads (shakers) exerted on the bearing housing. Note that structural cross-coupling effects are minimal for the present test rig configuration. For reasons that will become apparent later, Table 1 also introduces estimation for the lubricant mass filling the volume in the housing just above the thin film region, i.e. prior to the hydrodynamic film region.

Table 1. Physical parameters of bearing test section for dry (no lubricant) conditions

		SI Units		English	Units
	Symbol	x-direction	y-direction	x-direction	y-direction
Structural stiffness	$(K_s)_{x,y}$	832.3 kN/m	844.2 kN/m	4756 lb/in	4824 lb/in
Natural frequency	$(f_n)_{x,y}$	49 Hz	50 Hz		
Equivalent mass	$(M)_{x,y}$	8.43 kg	8.55 kg	18.6 lb	18.8 lb
Damping ratio	$(\zeta)_{x,y}$	0.037	0.034		
Damping coefficient	$(C_s)_{x,y}$	196 Ns/m	183 Ns/m	1.1 lb.s/in	1.0 lb.s/in
Estimated mass of lubricant on housing feed plenum (*)	M_f	0.35 kg	0.35 kg	0.77 lb	0.77 lb

Uncertainty in stiffness measurement 12 kN/m. Uncertainty in natural frequency 0.4 Hz

(*) Estimation derived from drawings of bearing assembly.

The lubrication system includes a sump tank (150 liter) and a frequency controlled main pump for supply of lubricant to the test bearing section and ball bearings supporting the shaft. An electric heater and thermostat control are located at the discharge of the main pump with a recirculation line. The heater warms the lubricant in the tank to a preset temperature prior to testing. A flexible hose delivers the lubricant to the top of the bearing test section. Secondary pumps evacuate (suction) lubricant after discharge from the test section and ball bearings, and return the lubricant to the sump. The lubricant in the experiments is an ISO VG 2 oil whose density and viscosity are measured using a graduated vessel and weight scale and a viscometer[2], respectively. The lubricant density (ρ) is 736 kg/m^3, and its absolute viscosity follows the following exponential relationship with temperature (°C):

$$\mu_{oil}(T) := 3.03\,e^{-.0209 \cdot (T-23.6)} \quad \text{cPoise} \tag{1}$$

EXPERIMENTAL PROCEDURE

The original design called for multiple frequencies (sine-sweep) force excitations to rapidly implement the frequency domain identification methods developed [6] earlier and forward bearing parameters (force coefficients) over selected frequency ranges for various shaft speeds and other operating conditions (lubricant feed pressure and temperature). However, the test bearing is of a large size and fluid film bearing reaction forces could easily exceed the load capacity of the shakers (max. 100 N [20 lb])[3].

Thus, the experiments for identification of squeeze film parameters are conducted with single-frequency (periodic) loads to maximize the force output from the shakers. Furthermore, three frequencies (40, 50and 60 Hz) around the "dry" system natural frequency are selected to make more apparent the effect of squeeze film damping on the bearing forced response.

The electromagnetic shakers excite the bearing along directions (X, Y) to produce bearing motions representing closely (a) centered and off-centered circular orbits, (b)

---

[2] Brand name: Mobil Velocite No. 3 oil. Viscosity measurements obtained with Rheology International RI:1:L Viscometer.

unidirectional motions along X- and Y-axes, and (c) elliptical motions with major axis $45°$ away from the X- and Y-axes. This last force condition is the most effective to maximize the load output from the shakers. Figure 6 depicts the types of dynamic motions induced on the bearing.

A PC controlled signal generator provides a fixed frequency, fixed voltage signal to the shakers. The amplitudes of load applied to the bearing are adjusted using the manual knob on each shaker power amplifier. In general, the applied forces are expressed as

$$F_x(t) = F_{xc}\cos(\omega t) + F_{xs}\sin(\omega t) = \left(F_{xc} - i F_{xs}\right)e^{i\omega t} = \overline{F}_x\, e^{i\omega t}$$

$$(2)$$

$$F_y(t) = F_{yc}\cos(\omega t) + F_{ys}\sin(\omega t) = \left(F_{yc} - i F_{ys}\right)e^{i\omega t} = \overline{F}_y\, e^{i\omega t}$$

The experiments are conducted with lubricant at three (inlet) temperatures and a supply pressure into the bearing plenum of just 0.07 bar (1 psig). Recorded through flow rates (Q_z) are approximately 0.7 LPM (11.7 cm^3/s) for most test conditions[4]. Table 2 presents a summary of the test conditions. Most importantly, the Table forwards the magnitudes of the measured bearing (diametric) clearance just before and after completing an experiment. Note that the (hot) lubricant flowed through the test section until a steady-state thermal condition is attained within the bearing.

Note that the recorded diametric clearances are smaller than the design value (0.254 mm) and significantly different in both directions (X and Y). The hot lubricant and warm housing and shaft cause the journal expansion, thus determining a net reduction in clearance. Note that the bearing clearance in the Y-direction is (consistently) ~ 10% larger than in the X-direction. The difference needs be accounted for in the appropriate prediction of hydrodynamic fluid film forces.

A data acquisition board[5] and PC [6]software collect measurements of (x, y) loads, bearing displacements and accelerations, and two film pressures. Data are recorded as

---

[3] Predictions also show large values of (with lubricant) damping coefficients that render a nearly overdamped structural system. Thus, single frequency dynamic forces will assure sustained motions of sufficient amplitude for reliable measurements.

[4] This flow rate indicates an axial pressure drop across the damper much lower than 1 psi. At the feed plenum, the pressure sensor uncertainty is +/- 1 psi.

[5] National Instruments 8-channel PCI-6052E board and LabView© ver 5.1

ASCII files for later processing using a MATHCAD® identification software developed by Dr. Luis San Andrés. In the data acquisition, the sampling rate is 2048 Hz with a total of 1024 recorded points. Thus, the total record time for each experiment is 0.5 s, sufficiently long to contain (at least) 20, 25 and 30 full periods of motion for excitations at 40, 50 and 60 Hz, respectively.

Table 2. Summary of tests and measured bearing (diametral) clearances before and after each test

Nominal (design) diametral clearance c=254 microns. Through flow rate (Q_z) ~ 0.7 LPM.
Acronyms: (**CC0**) circular centered orbits,
  (**CFx**) elliptical motions for force excitation along X-direction, $F_x > F_y$,
  (**CFy**) elliptical motions for force excitation along Y-direction, $F_y > F_x$,
  (**C45deg**): elliptical motions for force excitation 45 degrees from X-direction, $F_x = F_y$.

Test Description	*X - direction*		*Y - direction*		Inlet Temp (C)	Film 1 Temp (C)	Film 2 Temp (C)
	Clearance Before (microns)	Clearance After (microns)	Clearance Before (microns)	Clearance After (microns)			
CCO 100F	234	236	251	251	37	38	38
CCO 116F	213	213	231	229	46	47	47
CCO 130F	193	193	213	211	53	54	54
CFx 100F	236	236	249	249	37	38	38
CFx 116F	221	218	236	236	45	47	46
CFx 130F	193	196	211	213	53	54	54
CFy 116F	221	218	236	236	45	47	46
CFy 100F	236	236	249	249	37	38	38
CFy 130F	193	196	211	213	53	54	54
C45deg 100F	236	236	249	249	37	38	38
C45deg 116F	221	218	236	236	45	47	46
C45deg 130F	193	196	211	213	53	54	54

Notes:
  Inlet temperature: thermocouple immersed in plenum just above hydrodynamic film.
  Film 1 and 2 temperatures recorded within hydrodynamic film (axial length) near top and bottom, respectively.
  Test bearing section allowed to reach steady state at the above measure temperatures. The "before" measurements of clearance are conducted once steady state is achieved.
  Feed (supply) pressured (~ 1psig) recorded by static pressure gauge mounted at inlet of test section.
  Flow rate measured by recording time for accumulation of lubricant within a fixed volume (0.5 liters).

---

[6] Program LabView© SFDCCO developed by Dr. Sergio Diaz for the Rotordynamics Laboratory (July 2001).

PROCEDURE FOR IDENTIFICATION OF BEARING FORCE COEFFICIENTS

The identification procedure follows a well known method for estimation of system parameters from orbital journal motions induced by single frequency forcing functions [7]. The equations of motion for the test bearing section are

$$\begin{bmatrix} M+M_f & 0 \\ 0 & M+M_f \end{bmatrix}\begin{Bmatrix} \ddot{x} \\ \ddot{y} \end{Bmatrix}+\begin{bmatrix} K_{sx} & 0 \\ 0 & K_{sy} \end{bmatrix}\begin{Bmatrix} x \\ y \end{Bmatrix}=\begin{Bmatrix} F_x \\ F_y \end{Bmatrix}-\begin{Bmatrix} F_x \\ F_y \end{Bmatrix}_{Bearing} \tag{3}$$

where the bearing reaction forces are given by the linearized description

$$\begin{Bmatrix} F_x \\ F_y \end{Bmatrix}_{Bearing}=\begin{bmatrix} C_{xx} & C_{xy} \\ C_{yx} & C_{yy} \end{bmatrix}\begin{Bmatrix} \dot{x} \\ \dot{y} \end{Bmatrix}+\begin{bmatrix} D_{xx} & D_{xy} \\ D_{yx} & D_{yy} \end{bmatrix}\begin{Bmatrix} \ddot{x} \\ \ddot{y} \end{Bmatrix} \tag{4}$$

in terms of damping $\{C_{\alpha\beta}\}_{\alpha\beta=x,y}$ and inertia $\{D_{\alpha\beta}\}_{\alpha\beta=x,y}$ force coefficients. Recall that a squeeze film damper does not generate stiffness coefficients. Equation (3) includes the added mass of fluid (M_f) that accumulates in the plenum above the fluid film bearing. The analysis also disregards the "dry" damping coefficients $(C_s)_{x,y}$ since their magnitudes are a minute fraction of the (expected) squeeze film damping coefficients.

For periodic force excitations, as defined in equation (2), the bearing motions are also periodic with the same frequency (ω). Thus, the bearing displacements and accelerations are written as

$$\begin{Bmatrix} x \\ y \end{Bmatrix}=\begin{Bmatrix} x_c-ix_s \\ y_c-iy_s \end{Bmatrix}e^{i\omega t}=\begin{Bmatrix} \bar{x} \\ \bar{y} \end{Bmatrix}e^{i\omega t}\,;\quad \begin{Bmatrix} \ddot{x} \\ \ddot{y} \end{Bmatrix}=\begin{Bmatrix} \bar{a}_x \\ \bar{a}_y \end{Bmatrix}e^{i\omega t} \tag{5}$$

Substitution of equations (2), (4) and (5) into (3) renders the following[7]:

---

[7] Note that the model assumes the shaft remains static, i.e. without motions. Otherwise, the relationship $\ddot{x}=-\omega^2 x(t)$ between recorded (relative to shaft) displacements and bearing housing acceleration does not hold.

7

$$\begin{bmatrix} i\omega C_{xx}-\omega^2 D_{xx} & i\omega C_{xy}-\omega^2 D_{xy} \\ i\omega C_{yx}-\omega^2 D_{yx} & i\omega C_{yy}-\omega^2 D_{yy} \end{bmatrix} \begin{Bmatrix} \bar{x} \\ \bar{y} \end{Bmatrix} = \begin{Bmatrix} \bar{F}_x \\ \bar{F}_y \end{Bmatrix}_{Bearing}$$

(6)

$$\begin{Bmatrix} \bar{F}_x \\ \bar{F}_y \end{Bmatrix}_{Bearing} = \begin{Bmatrix} \bar{F}_x \\ \bar{F}_y \end{Bmatrix} - \begin{bmatrix} M+M_f & 0 \\ 0 & M+M_f \end{bmatrix} \begin{Bmatrix} \bar{a}_x \\ \bar{a}_y \end{Bmatrix} - \begin{bmatrix} K_{xx} & 0 \\ 0 & K_{yy} \end{bmatrix} \begin{Bmatrix} \bar{x} \\ \bar{y} \end{Bmatrix}$$

Analysis of the measurements reveals that, except for the largest amplitudes of motion due to large applied forces, the bearing does not show cross-coupled effects. Furthermore, the recorded pressures do not evidence fluid film cavitation[8]. In this case, the squeeze film bearing generates only direct force coefficients, i.e. $C_{xy}=C_{yx}=D_{xy}=D_{yx}=0$. This consideration allows further simplification (uncoupling) of the identification equations to the simple formula:

$$\left(C_{xx}+i\omega D_{xx}\right)=\frac{\bar{F}_x-K_{xx}\bar{x}-(M+M_f)\bar{a}_x}{i\omega\bar{x}};$$

(7)

$$\left(C_{yy}+i\omega D_{yy}\right)=\frac{\bar{F}_y-K_{yy}\bar{y}-(M+M_f)\bar{a}_y}{i\omega\bar{y}}$$

Each of Equations (7) is complex in character, i.e. contains a real part and an imaginary part, thus allowing direct evaluation of the squeeze film damping and inertia force coefficients at the excitation frequency (ω).

A MATHCAD worksheet processes the test data and forwards the force coefficients. The worksheet first converts the recorded voltage signals into appropriate physical units, stacks the date representing measurements conducted for increasing (applied) loads, proceeds to identify the (fundamental) Fourier coefficients of the displacements, accelerations and forces (see equation 2), and extracts the parameters using equation (7). Graphical output is readily available and includes comparisons with theoretical predictions.

---

[8] However, air ingestion was evident throughout the entire testing, being more pervasive at moderately large amplitudes of motion and the largest frequency of excitation. A discussion on this phenomenon and its effect on the identified bearing coefficients follow later.

PREDICTIONS BASED ON THE SHORT LENGTH BEARING MODEL

Analytical expressions for the bearing damping and inertia force coefficients are readily available for an open-ended, short length, squeeze film damper model. Table 3 presents the (generally accepted) expressions for prediction of damper force coefficients [8, 9]. Note that the expressions below are applicable to a full film cylindrical bearing of uniform radial clearance.

Table 3. Theoretical damping and inertia force coefficients for full film short length squeeze film damper

Circular centered motions $\varepsilon = e/c$	Damping	$C_{xx} = C_{yy} = C_{rr} = \dfrac{\pi \mu D}{2(1-\varepsilon^2)^{3/2}}\left(\dfrac{L}{c}\right)^3$
(r,t): radial and tangential coordinates	Inertia	$D_{xx} = D_{yy} = D_{rr} = \dfrac{\pi \rho D}{12}\left(\dfrac{L^3}{c}\right)\left[1-2(1-\varepsilon^2)^{1/2}\right]\left\{\dfrac{(1-\varepsilon^2)^{1/2}-1}{\varepsilon^2(1-\varepsilon^2)^{1/2}}\right\}$
Unidirectional *(x)* motions about a static equilibrium position $\varepsilon = e_x/c$	Damping	$C_{xx} = \mu D\left(\dfrac{L}{c}\right)^3 \dfrac{\pi(1+2\varepsilon^2)}{2(1-\varepsilon^2)^{5/2}}$
		$C_{yy} = \mu D\left(\dfrac{L}{c}\right)^3 \dfrac{\pi}{2(1-\varepsilon^2)^{3/2}}$
	Inertia	$D_{xx} = \dfrac{\pi \rho D}{12}\left(\dfrac{L^3}{c}\right)\dfrac{\left[1-(1-\varepsilon^2)^{1/2}\right]}{\varepsilon^2(1-\varepsilon^2)^{1/2}}$
		$D_{yy} = \dfrac{\pi \rho D}{12}\left(\dfrac{L^3}{c}\right)\dfrac{\left[1-(1-\varepsilon^2)^{1/2}\right]}{\varepsilon^2}$

(L, D, c) denote the damper axial length, diameter and radial clearance, respectively, *(μ,ρ)* are the lubricant viscosity and density. $\varepsilon = e/c$ represents the dimensionless orbit radius for circular centered motions, or the dimensionless static (off-center) position for unidirectional journal motions. The model assumes an isoviscous and incompressible lubricant, low magnitudes of external pressurization, and most importantly a squeeze film **fully submerged in a lubricant bath.**

Figure 7 displays theoretical predictions for the damping and inertia coefficients applicable to circular centered motions (C_{rr}, D_{rr}) and unidirectional *x*-motions $(C_{xx}, D_{xx}$,

C_{yy}, D_{yy}^{1} about an off-centered journal position. The predictions show damping coefficients increasing rapidly (nonlinear) as the orbit radius increases or as the dynamic amplitude of journal x-motion increases. The inertia force coefficients at the journal centered position equal 1.80 kg. For circular centered orbits, the inertia coefficient (D_{rr}) decreases as the orbit grows due to fluid advection effects [8]. On the other hand, the coefficients for unidirectional motions (D_{xx}, D_{yy}) may increase or decrease, depending on whether the coefficient represents a force/acceleration ratio along or orthogonal to the x-axis [9].

In Figure 7, the damping coefficients are based on a damper effective length (L_e), typically 80% of the design length. The rationale for using an effective length follows later in the discussion of air entrainment effects. The inertia coefficients are based on the damper length (L) though.

The test bearing stiffness and mass (see Table 1) render a system critical damping coefficient, $2\,(K_s\,M)^{1/2}$, equal to 5,300 Ns/m. Thus, the lowest predicted value of the lubricated film damping coefficient ($\sim$ 4,470 Ns/m [25.5 lb.s/in]) renders a viscous damping ratio (ζ) equal to 0.84, denoting an almost critically damped system. Thus, then the reason to induce single-frequency excitation forced motions to enable a measurable test bearing response with the current shakers.

EXPERIMENTAL RESULTS AND COMPARISON TO PREDICTIONS

Figures 9 through 25 depict the results of the measurements (forces, displacements and accelerations) and identified force coefficients for the different forced excitations exerted on the test bearing. Comparisons with damping predictions based on the short length bearing model use effective lengths (L_e) equal to 82%, 80% and 78% of the design length (L) for whirl frequencies 40, 50 and 60 Hz, respectively. The section on air entrainment effects provides the rationale for the estimation of the effective film land length.

Force coefficients for circular centered orbits

Figures 8 through 10 depict the test results for experiments conducted with a lubricant temperature of 38 °C (100 °F) and increasing frequencies equal to 40, 50 and 60 Hz,

respectively. The top graphs in Figure 8 display the applied forces $(F_y \text{ vs } F_x)$ and recorded orbital motions $(y \text{ vs. } x)$. Note that the bearing motions show random noise (spikes) probably caused by a faulty ground in the displacement sensors instrumentation. However, the noise does not affect the amplitude of motion at the excitation frequency. Figures 8 through 10 also include the amplitudes of the applied forces and the ensuing bearing amplitudes of motion revealing circular centered motions.

In the experiments, as the frequency of excitation increases it is more difficult to attain larger amplitudes of motion and orbital conditions closely resembling circular centered orbits. The maximum attainable shaker load (~ 120 N) then produces orbital motions with amplitudes of motion decreasing from 60 μm to 45 μm for frequencies ranging from 40 Hz to 60 Hz. The amplitudes of motion shown include peak x- and y- displacements, and the major (a) and minor (b) axes of the ellipses formed. Variations in these last two amplitudes show deviations from true circular orbits.

Figures 8 through 10 depict the identified damping (C_{XX}, C_{YY}) and inertia[9] $(M_{XX}, M_{YY})\omega$ coefficients versus the amplitude of dynamic bearing motion for increasing frequencies. Damping coefficients are virtually identical in both directions, x and y, and increase as the amplitude of motion increases. Excellent correlation with theoretical predictions based on an effective bearing length follow. The identified inertia coefficients are nearly independent of the amplitude of motion and about twice as large as the predicted inertia coefficients. For example, the theoretical inertia coefficient for small amplitude motions about the centered position ($D_{rr} = \dfrac{\pi \rho D L^3}{24 C}$) renders a magnitude of 3.28 kg, while the identification process delivers magnitudes equal to 6.5 kg and 6.3 kg at 40 Hz and 60 Hz, respectively. Note that this discrepancy is typical, see for example [10,11], and probably due to the type of boundary conditions in the test bearing, namely one end open to a flooded (feed) plenum and the other end open to ambient.

Figures 11 and 12 show the test damping (C_{XX}, C_{YY}) and inertia $(M_{XX}, M_{YY})\omega$ coefficients for experiments conducted with lubricant temperatures of 47 °C (116 F) and 54 °C (116 F), respectively. Each figure contains the coefficients for excitation

---

[9] The product of the inertia coefficient times the excitation frequency [rad/s] renders physical dimensions similar to that of damping. This representation reduces the number of figures depicting the test results.

frequencies equal to 40, 50 and 60 Hz. Predicted damping coefficients show a more nonlinear character at the largest amplitudes of motion. The (x- and y-direction) test coefficients are dissimilar, in particular at the largest frequency. Note again that experimentally derived inertia coefficients are ~ 200% larger than theoretical values.

In general, for circular centered motions, the predicted damping coefficients correlate well with the test values if an effective length (L_e) is used in the model. Otherwise, discrepancies would be more notable as discussed later. Inertia force coefficients appear insensitive to the amplitude of motion with magnitudes much larger than theoretical predictions for open ends SFD.

Force coefficients for elliptical orbits, X and Y directions

Figure 13 shows the forces and motions (x vs. y), amplitudes of force and motion (x, y) for elliptical orbits with the major amplitude along the X-axis. The test conditions are 40 Hz and lubricant supplied at 38 °C (100 °F). The graphs show amplitudes of motion increasing as the magnitude of the excitation force increases, until the maximum permissible with the current shaker arrangement. The largest amplitude of dynamic motion reaches ~ 70 μm, i.e. about 50% of the bearing radial clearance.

Figures 14 through 22 present the identified force coefficients for elliptical motions with major amplitudes of motion directed along the X-axis (top) and along the Y-axis (bottom). In the top graphs $F_x >> F_y$, while in the bottom graphs $F_y >> F_x$. Figures 14-16 show the test force coefficients for a feed lubricant temperature equal to 38 °C (100 °F) [2.25 cPoise viscosity] and frequencies of 40, 50 and 60 Hz, respectively. Figures 17-19 and Figures 20-21 compile the force coefficients identified for lubricant temperatures equal to 47 °C (116 °F) [1.87 cPoise] and 54 °C (130 °F) [1.59 cPoise], respectively, and at the three test frequencies.

The damping force coefficients (C_{xx}, C_{yy}) are similar in magnitude and agree well with predictions for orbital motions of small amplitude (e < 30 μm). As the amplitude of motion increases, the damping coefficient along the principal direction of motion increases rapidly, while the orthogonal coefficient remains nearly invariant[10]. Predictions,

---

[10] For elliptical motions with major amplitude (a) aligned with the X-axis, $C_{xx} > C_{yy}$. Similarly, for ellipses along the Y-axis, $C_{yy} >> C_{xx}$

on the other hand, show a rapid nonlinear increase with amplitude of motion. This behavior is certainly atypical of the experimentally derived coefficients. Note also that the bearing (hot) clearances in the X-direction are (~ 10%) larger than in the orthogonal direction (Y), and thus contribute to the differences mentioned. The predictions are based on an average radial clearance though.

The differences ascertained are more prevalent for the damping coefficients derived from the experiments at the largest frequency (60 Hz) and lowest lubricant viscosity (highest temperature). Note Figure 22 in particular, on which damping coefficients decrease as the amplitude of motion grows. This peculiar behavior is due to air ingestion and entrapment within the squeeze film lands, as discussed later.

For small amplitude orbital motions, the test inertia force coefficients (D_{xx}, D_{yy}) are similar in magnitude, yet consistently higher than predictions. However, in most tests the coefficient D_{yy} $(> D_{xx})$ increases as the amplitude of dynamic motion increases, while D_{xx} decreases, irrespective of the type of elliptical motion (X- or Y-oriented ellipses). The noted peculiar behavior, in particular at the highest frequency, may be due to the onset of cross-coupled effects which, although not accounted for in the identification model, still could reveal themselves as part of the identified coefficient[11].

Force coefficients for elliptical orbits, 45° away from X and Y directions

Identical time descriptions for the excitation forces, $F_x(t) = F_y(t)$, render elliptical motions with major axis 45° away from the X- or Y-axes. Experiments following this condition maximize the force output from the shakers, i.e. nearly a 45% increase.

Figures 23, 24 and 25 present the identified force coefficients derived from 45° oriented elliptical motions for lubricant temperatures corresponding to 38, 47 and 54 °C, respectively. On each figure, the top, middle and bottom graphs depict test results for excitation frequencies equal to 40, 50 and 60 Hz, respectively. As expected, larger bearing amplitudes of motion are recorded, ranging from nearly 95 µm at 40 Hz to 60 µm at 60 Hz. The identified force coefficients show similar trends as those observed for the other two types of elliptical motions. Presently, the damping coefficients along both

---

[11] The reported inertia coefficient, say D_{xx}, may be thought as an equivalent coefficient representing the combination $(D_{xx} - C_{xy}/\omega)$, for example.

13

directions are virtually identical, i.e. $C_{xx}=C_{yy}$, even for large amplitude orbital motions. The inertia force coefficients also display a similar behavior ($D_{xx}=D_{yy}$) with a less pronounced decay as the dynamic amplitudes rise. Note that in the 45°-elliptical motions, larger forces and amplitudes of motion are apparent along each axis (X and Y), thus leading to a more reliable and consistent identification process.

In general, for elliptical motions, predicted damping coefficients based on (L_e) correlate well with the identified coefficients only for small amplitude motions about the centered condition. Theoretical damping coefficients grow rapidly as the amplitude of motion increases thus denoting a strong nonlinear behavior. On the other hand, experimentally derived damping coefficients show a moderate increase, and in some cases remain nearly invariant. Identified inertia force coefficients are sensitive to the amplitude of motion and show magnitudes much larger than theoretical predictions, in particular for small amplitude motions. Note also that the predictions show an opposite trend, i.e. D_{xx} and D_{yy} increasing as the orbit amplitude increases.

ASSESSMENT OF AIR ENTRAINMENT EFFECTS ON THE BEARING FORCED RESPONSE. NATURE OF THE DISCREPANCIES BETWEEN TEST PARAMETERS AND PREDICTIONS

The experimental results presented as damping and inertia force coefficients show distinctive trends related to the type of motion and the various frequencies and lubricant viscosity (film temperature) considered. In general, damping coefficients agree well with predictions derived from a conventional hydrodynamic lubrication models if a certain "effective length" ($L_e < L$) is used.

In the preliminary analysis of the test results, the effective length, varying between 82% to 78% of the actual film length, bridged the difference between theoretical predictions and experimental results,[12] thus allowing a degree of confidence for the "expected" results. However, firm understanding of the experimentally derived force coefficients was evidently lacking.

---

[12] The test bearing configuration, sensors' sensitivities (calibration) and signal conditioning were thoroughly checked (more than once) to remove the possibility of an error. Eventually, student and P.I. agreed to "blame" the difference into an actual (reduced) film length due to a faulty assembly process. The following discussion on air entrainment clarifies the issue.

Most importantly, visual observations of the dynamic film using a stroboscopic lamp revealed air ingestion producing striations (fingering) starting at the bearing open end and growing towards the feed end. The air entrainment became more pervasive as the amplitude of motion increased, and certainly, most persistent for motions at the highest frequency. Pictures were taken although of poor quality (see below).

Top

Bottom

Air entrainment

The measured squeeze film pressures at two axial locations in the bearing land reveal the early onset of air entrainment affecting the bearing dynamic forced response[13]. Figures 26 and 27 display (top and bottom) film pressures over a time spanning four periods of motion with a whirl frequency equal to 40 Hz and 60 Hz, respectively. The lubricant feed temperature corresponds to 54 °C. Peak (shaker) forces (x,y) and ellipse major and minor amplitudes (a, b) are noted. The graphs on each figure show the evolution of the film pressure as the forces and ensuing amplitudes of motion increase. Note that film pressures increase as the force amplitude increases yet their profile does not correspond to either a full film condition or a vapor cavitation condition. On the other hand, the pressure waves resemble closely those measured earlier under conditions of severe air entrainment or with a bubbly lubricant mixture [1, 2, 3]. Note that these pressure fields develop a characteristic uniform pressure zone when air striations (fingering) grow in size within the squeeze film lands [1].

Diaz and San Andrés [4] advance a simple criterion to determine the likelihood of air entrainment. A feed-squeeze flow parameter (γ) relates the lubricant flow rate Q_z to the dynamic change in volume within the squeeze film gap, i.e.

$$\gamma = \frac{Q_z}{\pi D L e \omega} \tag{8}$$

If $\gamma > 1$ then no air entrainment occurs, i.e. the through flow is sufficient to fill the volume change caused by the journal whirl motion. On the other hand, air ingestion and

---

[13] The top and bottom pressure transducers (PT) are located 11 mm and 22 mm below the feed end. That is, $L/3$ distance apart.

entrapment occurs if $\gamma<1$ and the bearing operates with an air in oil (non homogeneous) mixture. The lower the feed-squeeze parameter (γ), the more severe the degradation in damper forced performance.

Figure 28 shows the test axial flow rate (Q_z=0.7 LPM) and dynamic film volume change (Q_d) versus amplitude of dynamic motion. The feed-squeeze flow parameter (γ), also displayed, decreases rapidly as the motion amplitude grows since the through flow rate is in actuality very small. Thus, severe air entrainment effects are prevalent in most of the tests conducted. Reference [4] forwards an empirical correlation between γ and the amount of air entrained (β: volume concentration of air) in the lubricant, i.e.

$$\beta_{(\gamma)} = \left(1 + \frac{2\pi\gamma}{\gamma\left(2\sin^{-1}(\gamma) - \pi\right) + 2\sqrt{1-\gamma^2}}\right)^{-1} \tag{9}$$

Tao et al. [12] advance a semi-empirical formula for estimation of the effective viscosity of the lubricant bubbly mixture, i.e. $\mu_e = \alpha_{(\beta)}\mu$, with a viscosity fraction defined as

$$\alpha_{(\beta)} = \left(1 - \beta^3\right)\left(1 + \frac{\beta}{4}\right) \tag{10}$$

Figure 29 depicts results using equations (9) and (10), i.e. the air volume fraction (β) and viscosity fraction $\alpha(\beta)$ versus the feed-squeeze flow parameter (γ). The severity of air entrainment increases as $\gamma \to 0$.

Recall that damping coefficients $(C_{i,j})_{i,j=x,y}$ derived from the short length bearing model are proportional to the lubricant viscosity (μ) and the third power of the land length (L), i.e. $C_{i,j} \approx \mu L^3$. This fundamental relationship is modified to include the effect of air entrainment by introducing an effective (reduced) viscosity or (if desired) an effective length (L_e), i.e.

$$C_{i,j} \approx \alpha_{(\beta)}\mu L^3 \approx \mu L_e^3; \quad L_e = l_{(\beta)} L; \quad l_{(\beta)} = \alpha_{(\beta)}^{1/3} \tag{11}$$

16

Figure 30 displays, as a function of the amplitude of dynamic motions, predictions for (a) the air entrainment volume fraction (β), (b) the viscosity fraction $\alpha(\beta)$, and (c) the effective length fraction $l_{(\beta)}$ for increasing whirl frequencies. Note that the effect of air ingestion is more pronounced for the largest amplitudes and highest frequencies, as expected. Average values for the effective parameters over the entire range of dynamic motions (to 90 µm) are given below as:

Frequency	Viscosity fraction	Effective length fraction
(Hz)	α	l
40	0.677	0.842
50	0.610	0.810
60	0.556	0.782

Note that the average values for the effective length fraction (l) correspond well with those chosen to perform the predictions, i.e. 82%, 80% and 78% of the actual damper length (L).

CONCLUSIONS

Experiments evidencing the forced response of a test squeeze film damper for various dynamic load conditions are reported. PC controlled shakers exert single frequency loads and induce circular orbits and elliptical orbits of increasing amplitudes to 80% of the damper radial clearance (0.122 mm). Measurements of the applied loads, bearing displacements and accelerations permit identification of damping and inertia force coefficients for operation at three whirl frequencies (40, 50 and 60 Hz) and increasing lubricant temperatures (reduced oil viscosity). Measurements of film pressures at two axial locations in the damper reveal an early onset of air ingestion within the film thus affecting the bearing damping capability.

Identified damping force coefficients agree well with predictions based on the conventional short length bearing model if an effective length is used with well known formulae. The effective length ranges from 82% to 78% of the actual damper length as the whirl excitation frequency increases. Justifications for the reduced length (or reduced effective viscosity) follow from the prevalent test conditions with a small through flow

rate, not large enough to offset the dynamic volume changes due to the large amplitude whirl motions. The measurements and analysis thus show the pervasiveness of air entrainment, whose effect increases with the amplitude and frequency of the dynamic journal motions. Identified inertia coefficients are approximately twice as large as those obtained from predictions also based on the short length bearing model. The noted discrepancies are well known in the literature and may obey to the type of feed condition, i.e. one side pressurized.

Providing enough external pressurization to insure a sufficiently large lubricant flow rate can prevent air ingestion. However, the required flow rates may easily exceed practical requirements, in particular for large size dampers operating at high frequencies. Further constraints on the lubricant stored volume and weight make this option not applicable in air breathing jet engines, for example. Thus, persistent air ingestion and entrapment will continue to afflict the dynamic forced performance in open ended SFDs. Fortunately, the current understanding of the flow physics does enable the prediction of force coefficients with a certain degree of confidence.

18

REFERENCES

1   Diaz, S., and L. San Andrés, "Air Entrainment Versus Lubricant Vaporization in Squeeze Film Dampers: An Experimental Assessment of their Fundamental Differences," ASME Journal of Gas Turbines and Power, Vol. 123 (4), pp. 871-877, 2001.

2   Diaz, S., and L. San Andrés, "Reduction of the Dynamic Load Capacity in a Squeeze Film Damper Operating with a Bubbly Lubricant", ASME Journal of Gas Turbines and Power Vol. 121, pp. 703-709, 1999.

3   Diaz, S., and L. San Andrés, "Pressure Measurements and Flow Visualization in a Squeeze Film Damper Operating with a Bubbly Mixture," ASME Journal of Tribology, Vol. 124 (4), pp. 346-350, 2002.

4   Diaz, S. and L. San Andrés, L., "A Model for Squeeze Film Dampers Operating with Air Entrainment and Validation with Experiments," ASME Journal of Tribology, Vol. 123 (1), pp. 125-133, 2001.

5   Romero, F., and L. Rodriguez, "Identification Of Structural Parameters In Vertical Test Rig," Tribology Group, Internal Progress Report, December 2001.

6   Diaz, S., and L. San Andrés, "A Method for Identification of Bearing Force Coefficients and Its Application to a Squeeze Film Damper with a Bubbly Lubricant," STLE Tribology Transactions, Vol. 42 (4), pp. 739-746, 1999.

7   Diaz, S. and L. San Andrés, L., "Orbit-Based Identification of Damping Coefficients on Off-Centered Squeeze Film Dampers Including Support Flexibility," ASME Paper 2000-GT-0394.

8   Vance, J., "Rotordynamics of Turbomachinery," John Wiley and Sons, New York, 1988.

97 San Andrés, L. and Vance, J., "Force Coefficients for Open Ends Squeeze Film Dampers Executing Small Amplitude Motions About an Off-Centered Equilibrium Position," ASLE Transactions, Vol. 30 (1), pp. 63-68, 1987.

10 Robison, M., G. Arauz, and L. San Andrés, "A Test Rig for the Identification of Rotordynamic Coefficients of Fluid Film Bearings," ASME Paper 95-GT-431.

11 Rami, M.D., J.B. Roberts, and J. Ellis, "Determination of Squeeze Film Dynamic Coefficients from Experimental Transient Data," ASME Journal of Tribology, Vol. 109 (1), pp. 155-163, 1987.

12 Tao, L., S. Diaz, L. San Andrés, and K.R. Rajagopal, "Analysis of Squeeze Film Dampers Operating with Bubbly Lubricants" ASME Journal of Tribology, Vol. 122 (1), pp. 205-210, 2000.

APPENDIX A. SENSOR SENSITIVITIES FOR VERTICAL FLUID FILM BEARING TEST RIG

Sensor designation & Type	Max Range Serial #	Sensitivity S: Volts/Physical Unit	Bias amplifier gain (B) & DC offset	Final sensitivity S x B: Volts/Physical Unit
Load, X PCB load cell Model 208B02	Max: 445 N SN: 12422	.01274 Volts/Newton	Gain: X1 Offset: 0	.01274 Volts/Newton
Load, Y PCB load cell Model 208B02	Max: 445 N SN: 12468	.01141 Volts/Newton	Gain: X1 Offset: 0	.01141 Volts/Newton
Displacement X BN eddy current	SN: FEBU411730	.00808 Volts/micron	Gain: X1 Offset: 9.76 V	.00808 Volts/micron
Displacement Y BN eddy current	SN: FEBU411728	.008135 Volts/micron	Gain: X1 Offset: 6.22 V	.008135 Volts/micron
Accelerometer X PCB Model U353B33	Max: +/- 50 g SN: 25767	.1057 Volts/g	Gain: X10 Offset: 0	1.057 Volts/g
Accelerometer Y PCB Model U353B33	Max: +/- 50 g SN: 25768	.1084 Volts/g	Gain: X10 Offset: 0	1.084 Volts/g
Pressure transducer (Bottom - Bearing) Entran EPX-V03-100P-/0.91	Max: 6.89 bar SN: 99199121-D01	.01726 Volts/bar	Gain: X200 Offset: 0	3.452 V/bar
Pressure transducer (Top – Bearing) Entran EPX-V03-100P-/0.91	Max: 6.89 bar SN: 99199121-D04	.01813 Volts/bar	Gain: X200 Offset: 0	3.626 V/bar

Pressure 1 (bottom): Output unconditioned at ambient pressure - .0145 Volts – location 21 mm from top

Output after signal conditioner (X200 gain) = 2.837 V.

Pressure 2 (top):   Output unconditioned at ambient pressure: .0251 Volts - location 11 mm from top
Output after signal conditioner (X200 gain) = 4.910 V.

Measurements using LABVIEW software of 2 forces (X,Y), 2 displacements (X,Y), 2 accelerations (X,Y) and 2 film pressures.
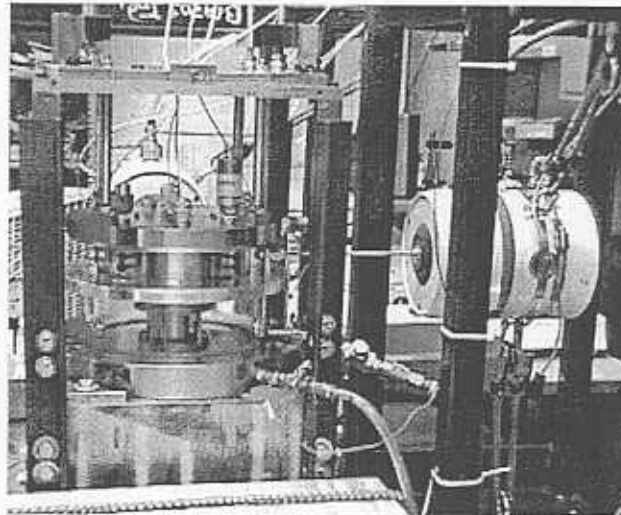
Figure 1. Test rig for dynamic force measurement of and flow visualization in plain journal bearing/SFD.
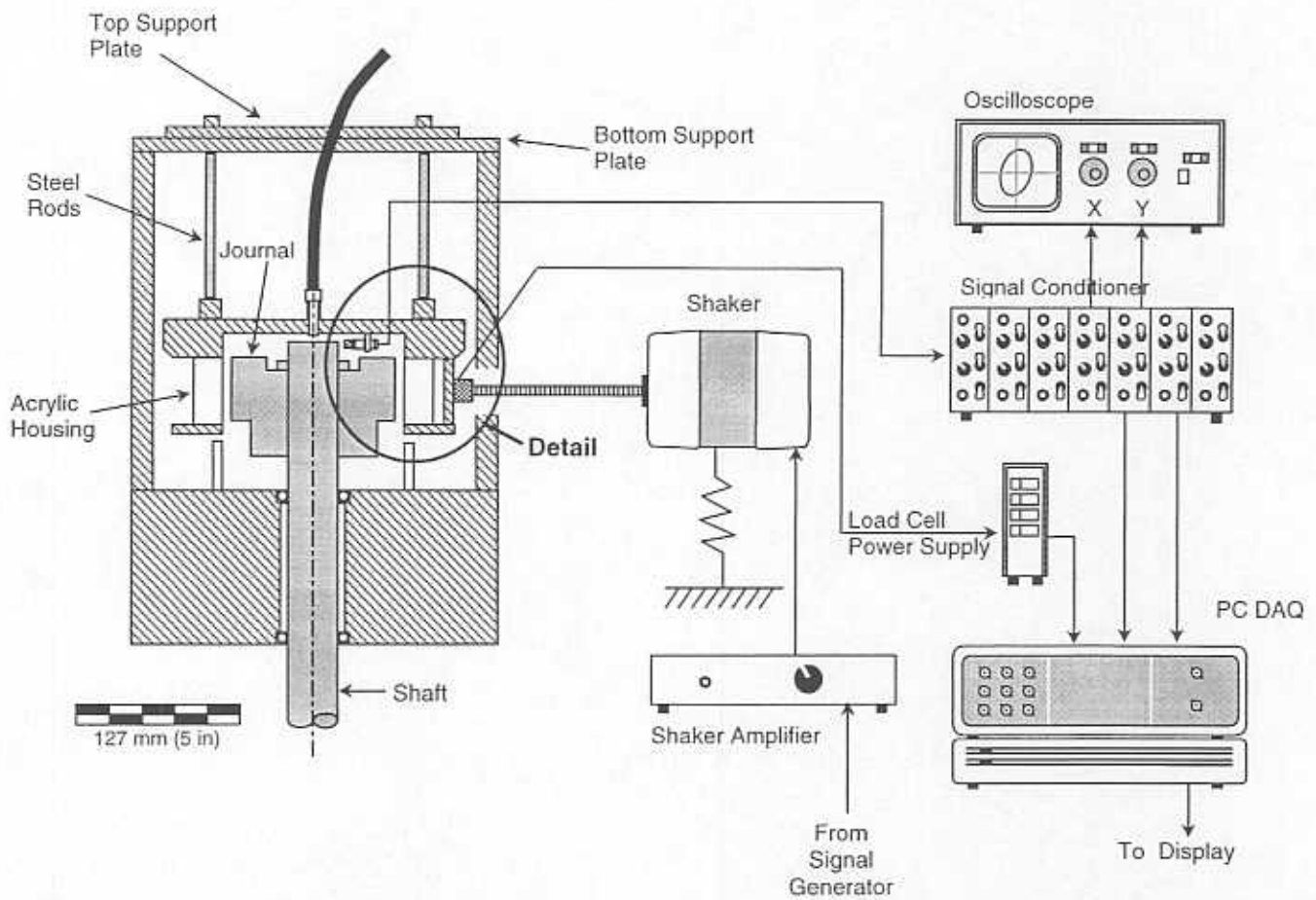
Figure 2. Cutaway view of the test rig for identification of fluid film bearing parameters.

21
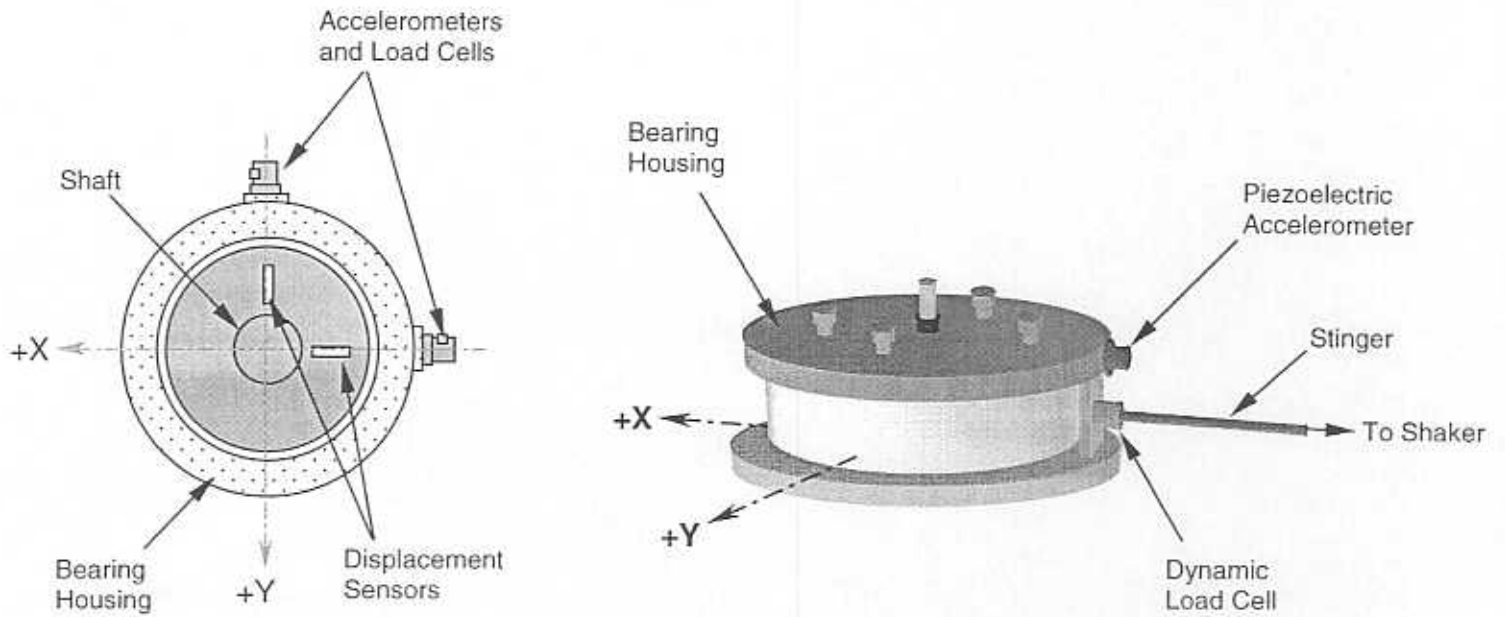
Figure 3. Positions of sensors and reference coordinate system.
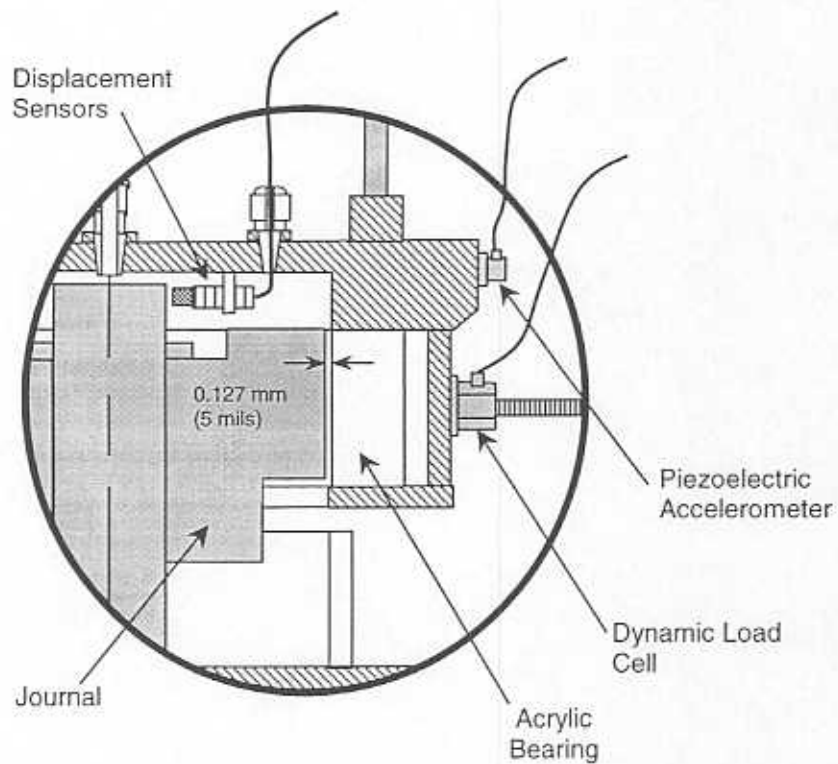
Figure 4. Detail of sensor disposition on bearing housing.

22

Static measurement - Structure
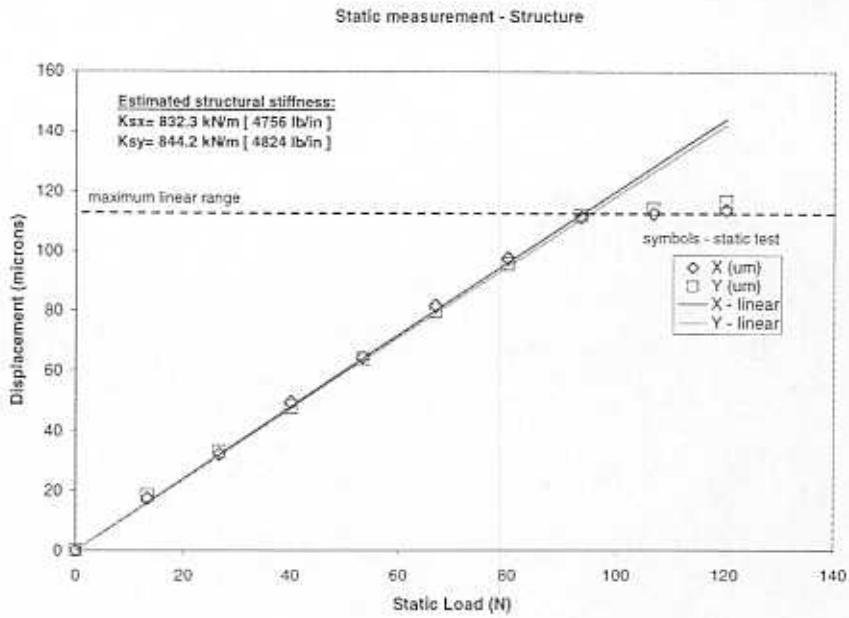
Figure 5. Identification of support structure stiffness from elastic deflections versus static loads.

Circular centered

Elliptical orbit – Y

Elliptical orbit – X

Elliptical orbit – 45
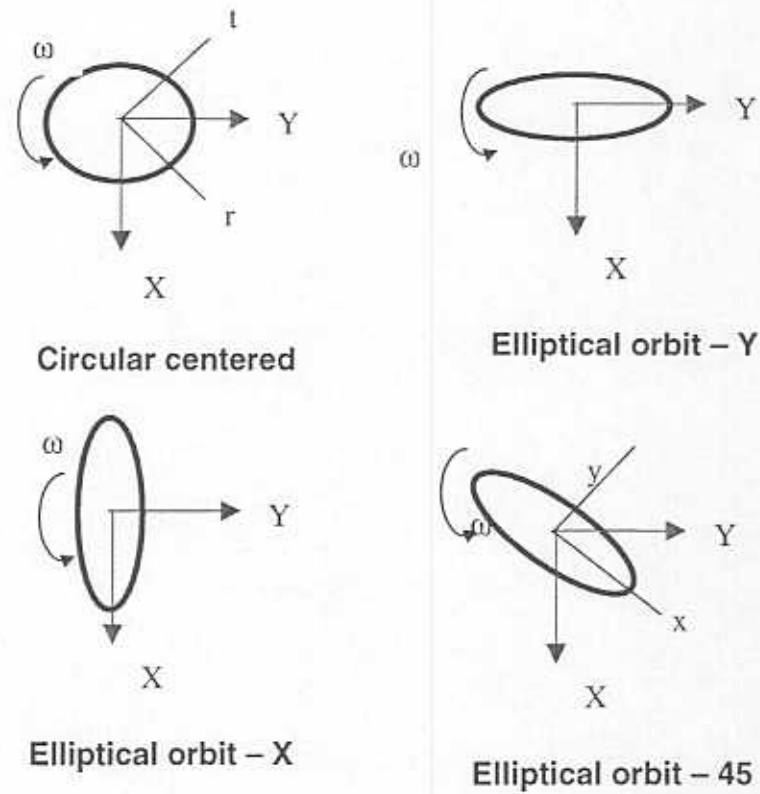
Figure 6. Types of dynamic bearing motions induced by external forces on test SFD.
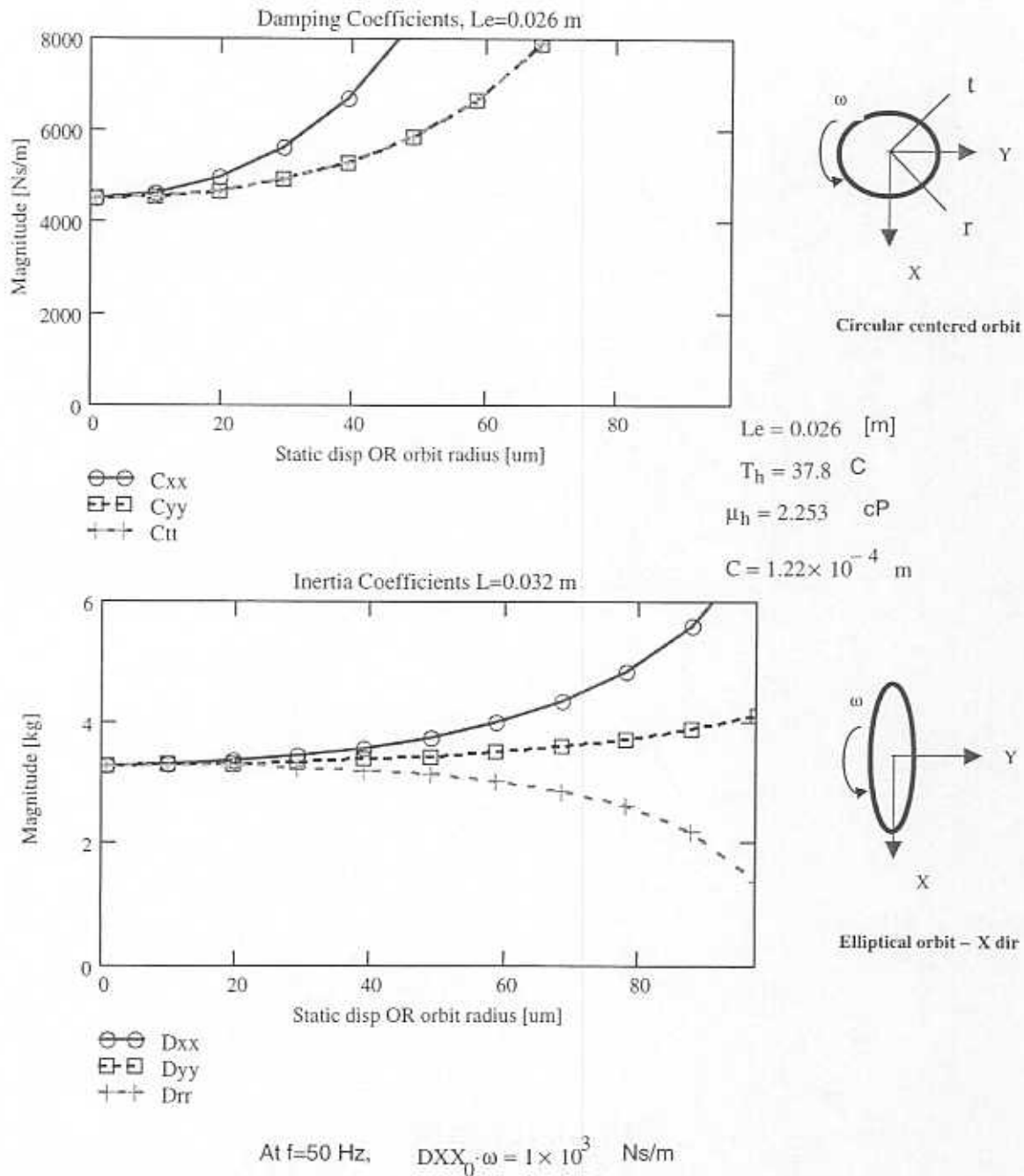
Figure 7. Predictions for damping and inertia force coefficients based on short length (full film) SFD model. Coefficients derived for circular centered orbits and off-centered unidirectional motions. Effective axial length used, other parameters noted.

24

Amplitude of forces and motion for circular centered orbits.
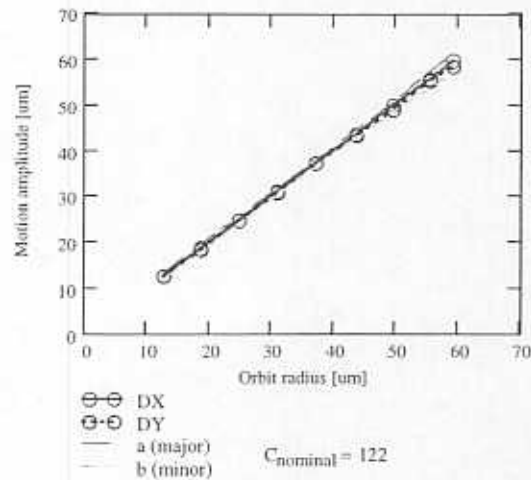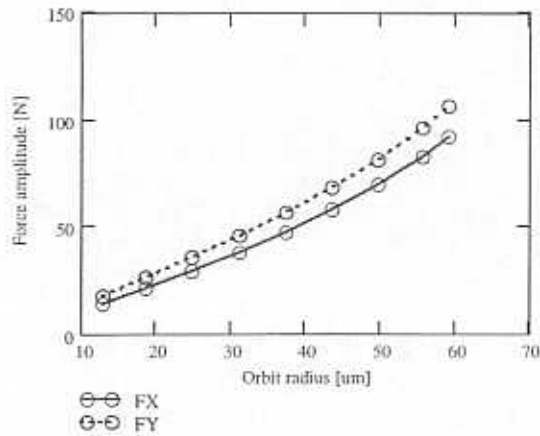
$C_{nominal} = 122$

Identified and Predicted Coefficients

$Le = 2.624 \times 10^{-2}$ [m]

$f = 40$ Hz

$T_h = 37.778 °C$

$\mu_h = 2.253 cP$

$C_{nominal} = 122$ μm

Figure 8. Test forces and motions (*X vs. Y*), amplitudes of force and motion (*X, Y*), identified and predicted (*C_{XX}, C_{YY}*) and inertia (*D_{XX}, D_{YY}*) ω force coefficients for circular centered orbits. Test conditions: 40 Hz, 38 °C, radial clearance (hot) 122 um.

25

Amplitude of forces and motion for circular centered orbits.

θ—θ FX
θ·θ FY

θ—θ DX
θ·θ DY
—— a (major)
-- b (minor)

$C_H = 122$ μm

Identified & Predicted Coefficients

$Le = 2.688 \times 10^{-2}$ m

$f = 50$ Hz

$T_h = 37.778$ C

$\mu_h = 2.253$ cP

$C_H = 122$ μm

O O Cxx
□ □ Cyy
—— Ctt - theory
O O Dxx w
□ □ Dyy w
—— Drr w - Theory
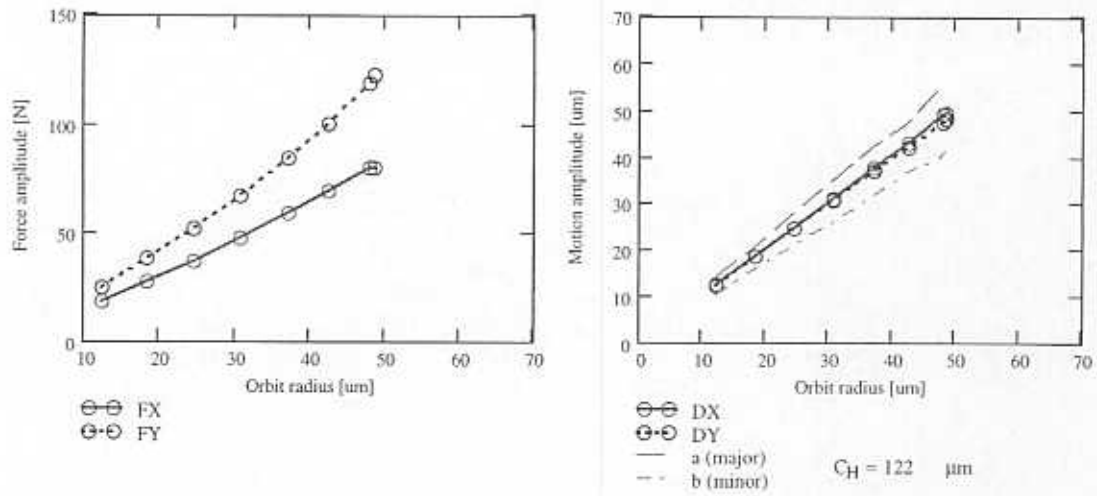
Figure 9. Test amplitude forces and motions *(X, Y)* and identified damping *(C_XX, C_YY)* and inertia *(D_XX, D_YY)ω* force coefficients for circular centered orbits. Test conditions: 50 Hz, 38 C, radial clearance (hot) 122 um. Predicted coefficients from short length SFD model.

Amplitude of forces and motion for circular centered orbits.

Identified & Predicted Coefficients

$L_e = 2.688 \times 10^{-2}$

$f = 60 \, Hz$

$T_h = 37.778 \quad C$

$\mu_h = 2.253 \quad cP$

$C_H = 122 \quad \mu m$
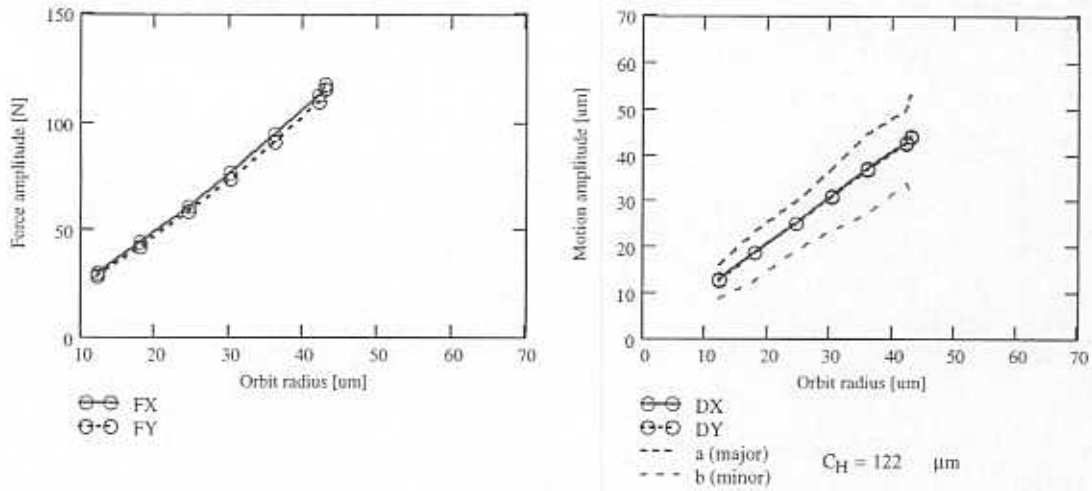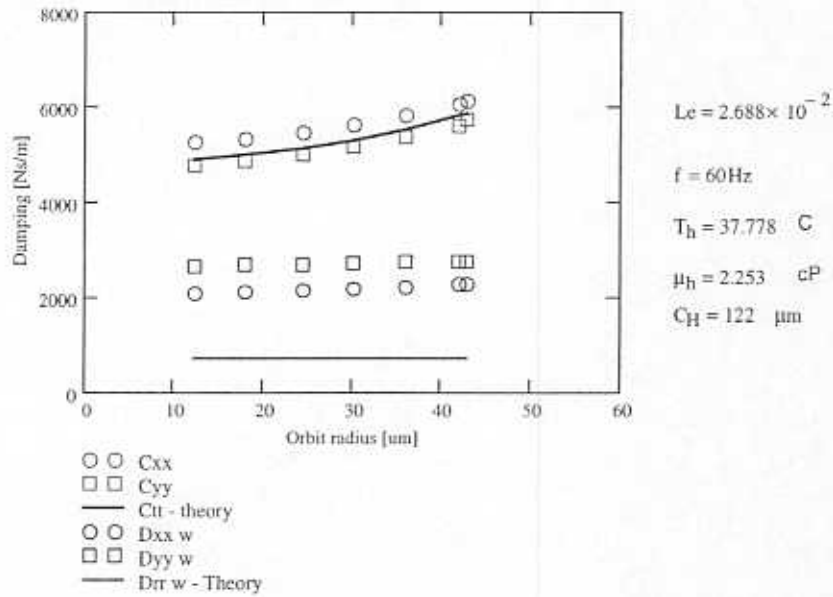
Figure 10. Test amplitude forces and motions *(X, Y)* and identified damping *(C_XX, C_YY)* and inertia *(D_XX, D_YY)* ω force coefficients for circular centered orbits. Test conditions: 60 Hz, 38 C, radial clearance (hot) 122 um. Predicted coefficients from short length SFD model.
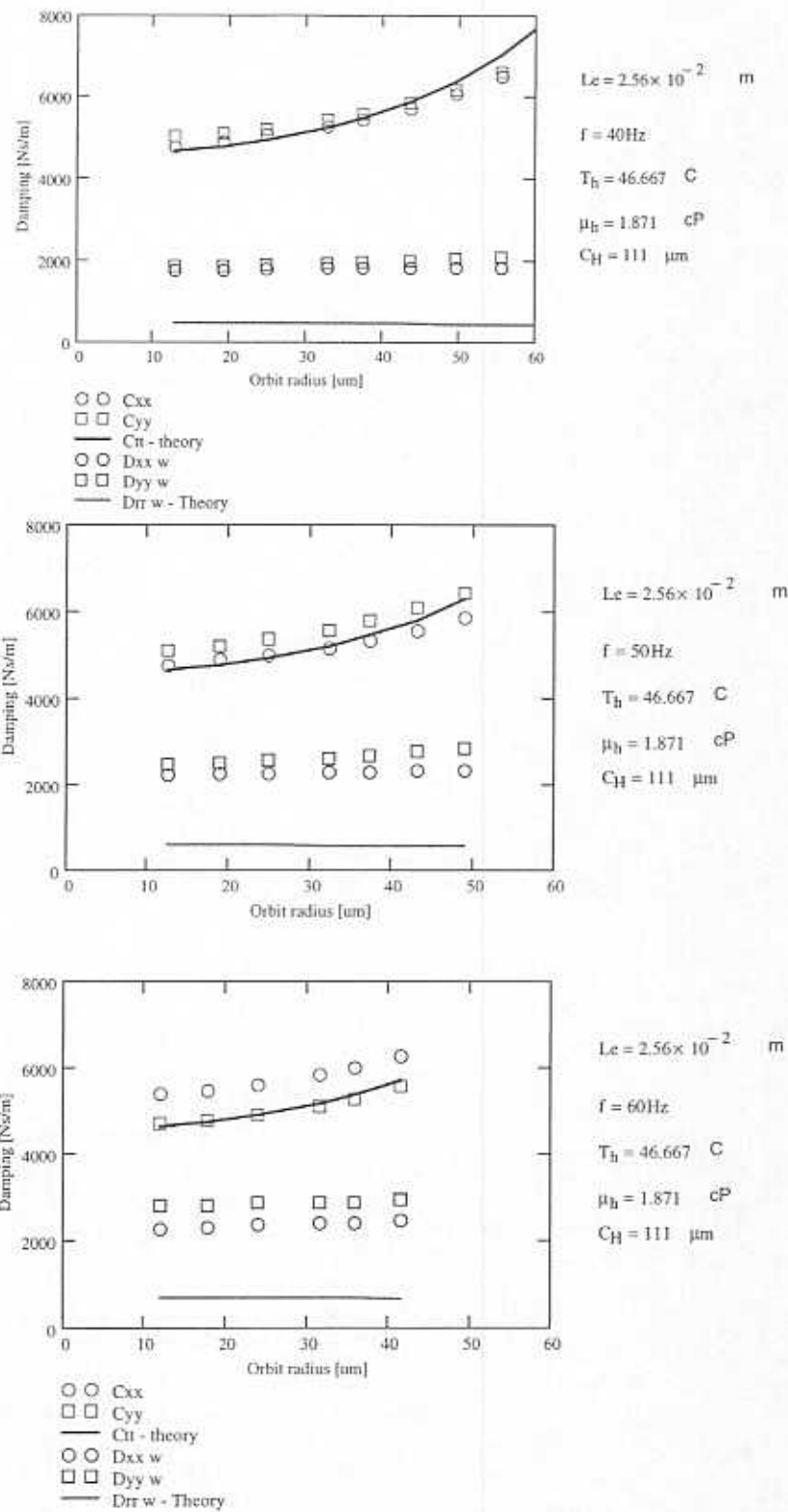
Figure 11. Test and predicted direct damping (C_{XX}, C_{YY}) and inertia coefficients (D_{XX}, D_{YY})ω for circular centered orbits. Test conditions: 40: 50: 60 Hz, 47 C, radial clearance (hot) 111 um.
Predicted coefficients from short length SFD model
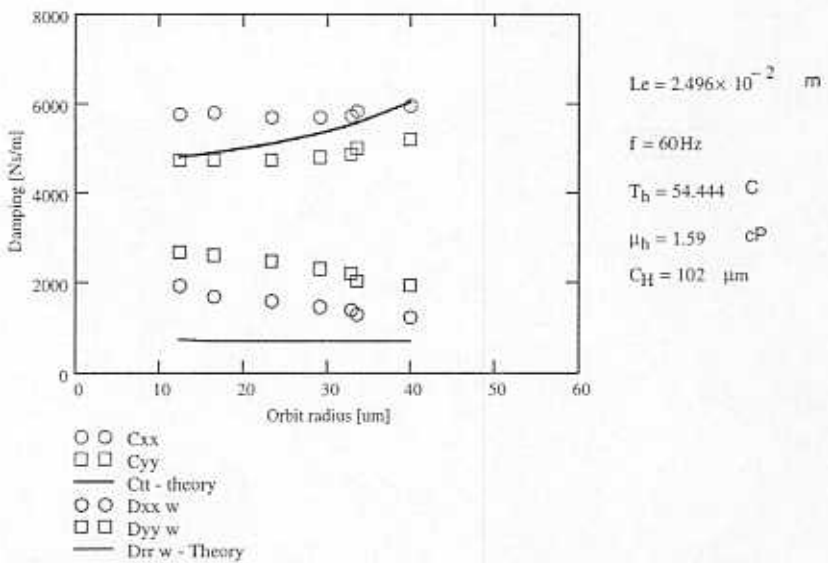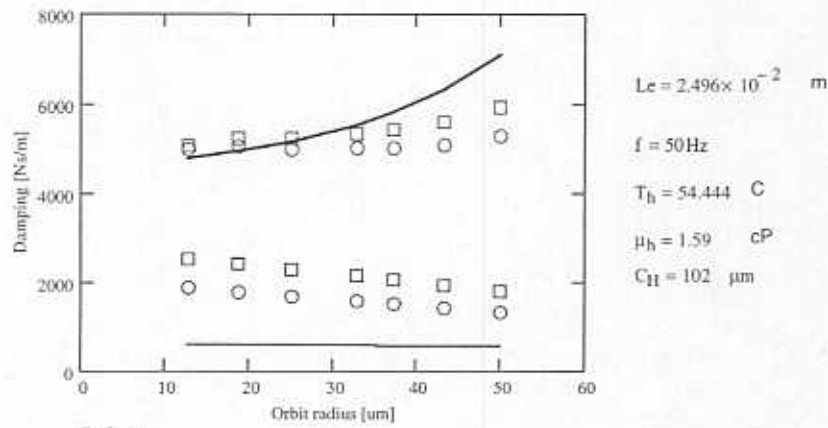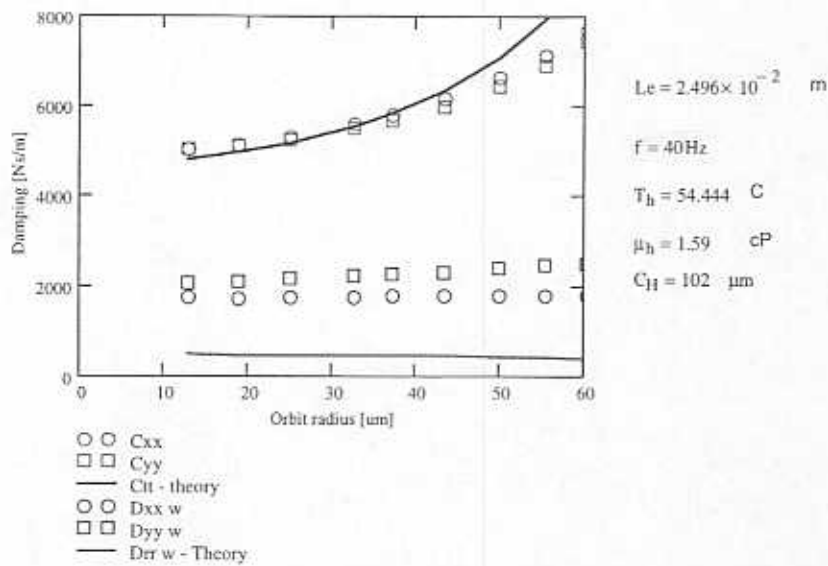
Figure 12. Test and predicted direct damping (C_{XX}, C_{YY}) and inertia coefficients (D_{XX}, D_{YY})ω for circular centered orbits. Test conditions: 40: 50: 60 Hz, 54 C, radial clearance (hot) 102 um. Predicted coefficients from short length SFD model.
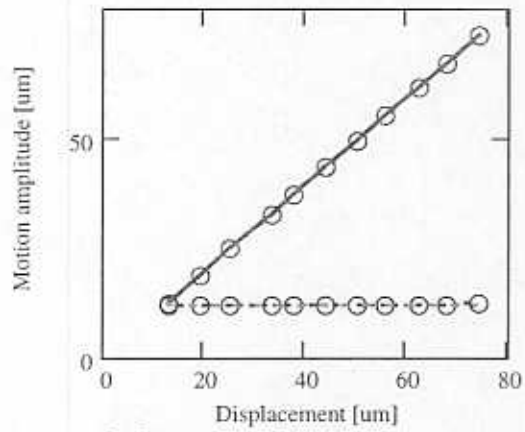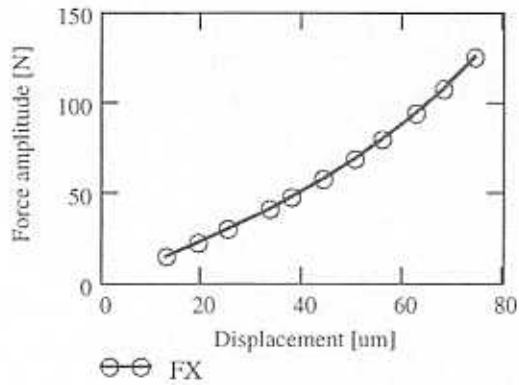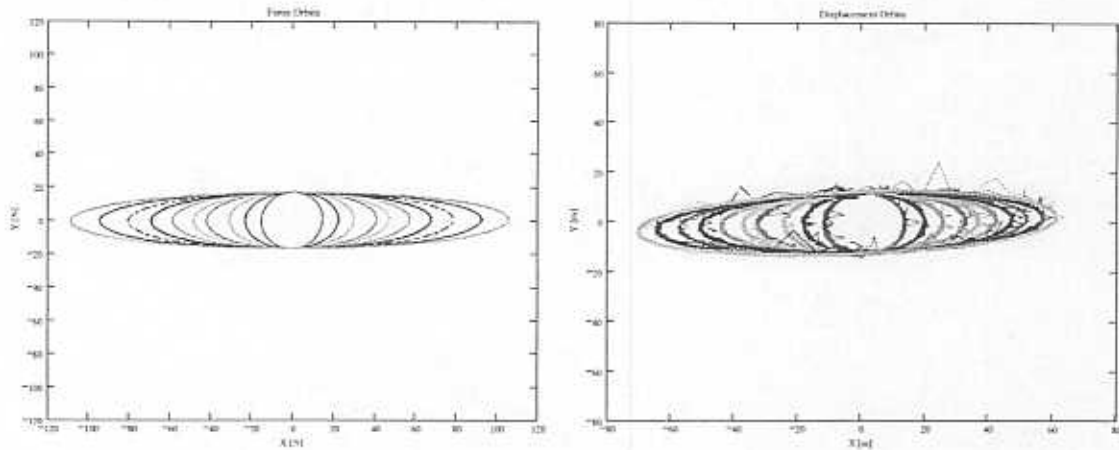
Force X and Orbital displacements (X,Y)

Figure 13. Test forces and motions (*X vs. Y*), amplitudes of force and motion *(X, Y)* for elliptical orbits. Major amplitude along *X*-axis. Test conditions: 40 Hz, 38 °C, radial clearance (hot) 122 um.
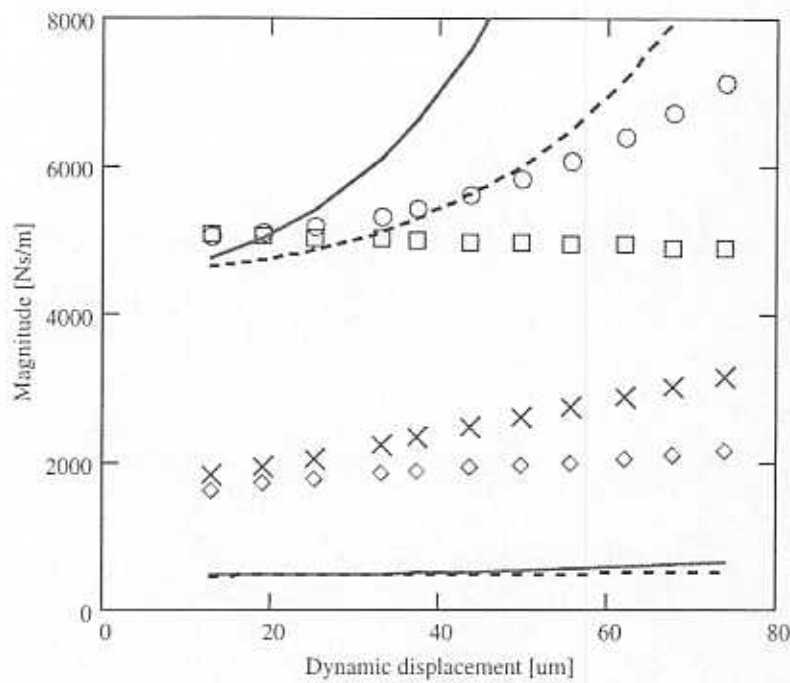
FX > FY

Le = 0.026 [m]

ω = 40   Hz

T_h = 37.8   C

μ_h = 2.25   cP

C_H = 121 μm

FY > FX

Le = 0.026 [m]

ω = 40   Hz
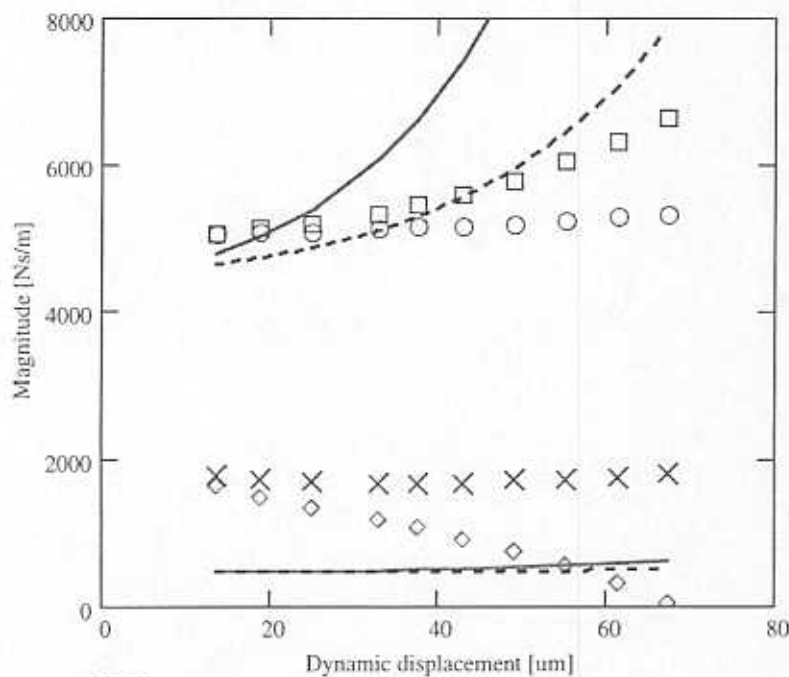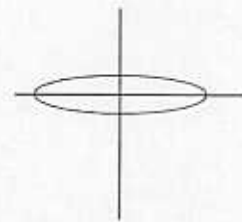
T_h = 37.8   C

μ_h = 2.25   cP

C_H = 121 μm
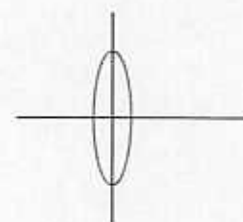
○ ○ Cxx
□ □ Cyy
—— C-d (theory)
- - - C-c (theory)
◇   Dxx w
✕ ✕ Dyy w
—— D-d (theory)
- - - D-c (theory)

Figure 14. Test and predicted direct damping (C_{XX}, C_{YY}) and inertia $(D_{XX}, D_{YY})\omega$ coefficients for elliptical motions; (top) $F_X > F_Y$, (bottom) $F_Y > F_X$. Test conditions: 40 Hz, 38 C, radial clearance (hot) 121 um. Predicted coefficients from short length SFD model.

31
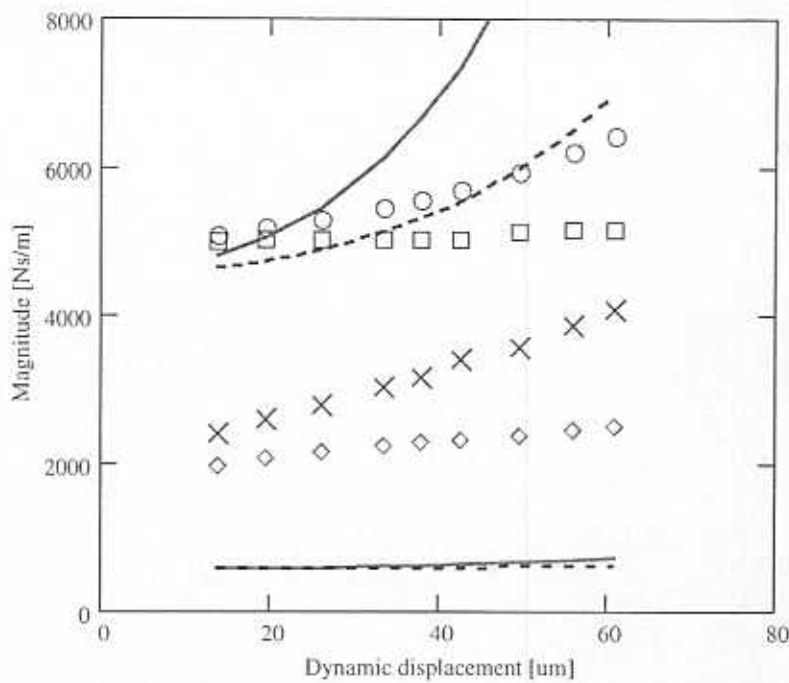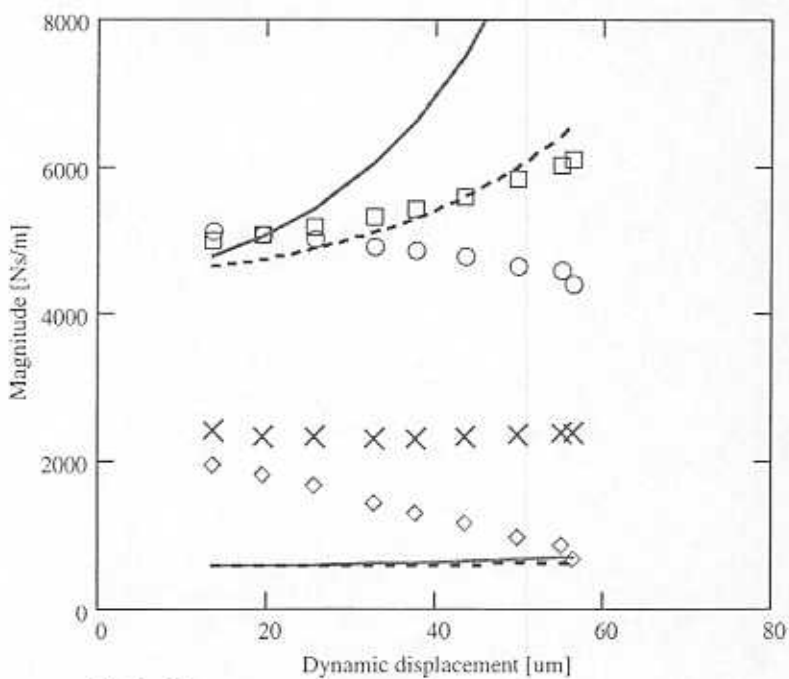
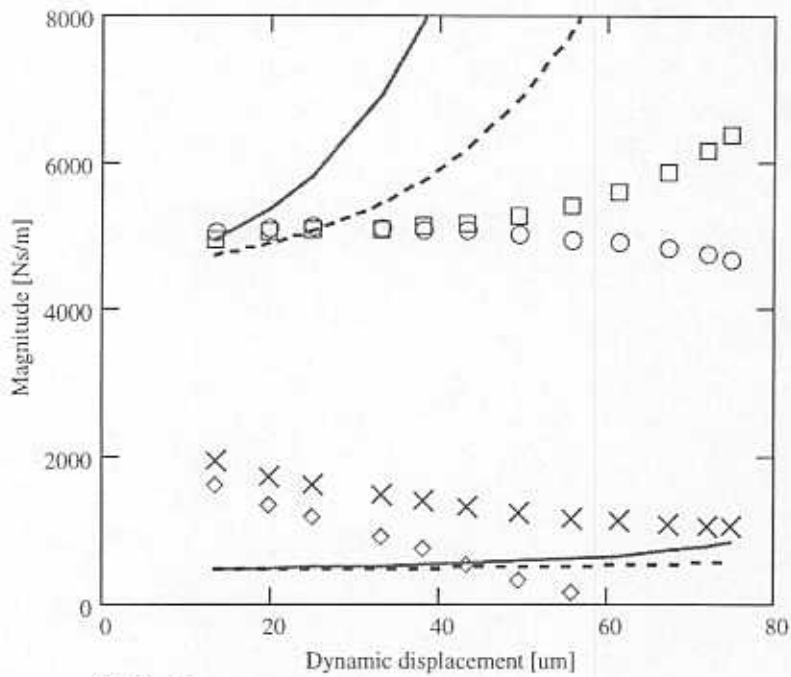Figure 15. Test and predicted direct damping (C_{XX}, C_{YY}) and inertia (D_{XX}, D_{YY})ω coefficients for elliptical motions; (top) $F_X > F_Y$, (bottom) $F_Y > F_X$. Test conditions: 50 Hz, 38 C, radial clearance (hot) 121 um. Predicted coefficients from short length SFD model.

Fx> Fy

Le = 0.026 [m]

ω = 60   Hz

T_h = 37.8 C

μ_h = 2.25 cP

C_H = 121   μm

Fy> Fx

Le = 0.026 [m]

ω = 60   Hz

T_h = 37.8 C

μ_h = 2.25 cP

C_H = 121   μm
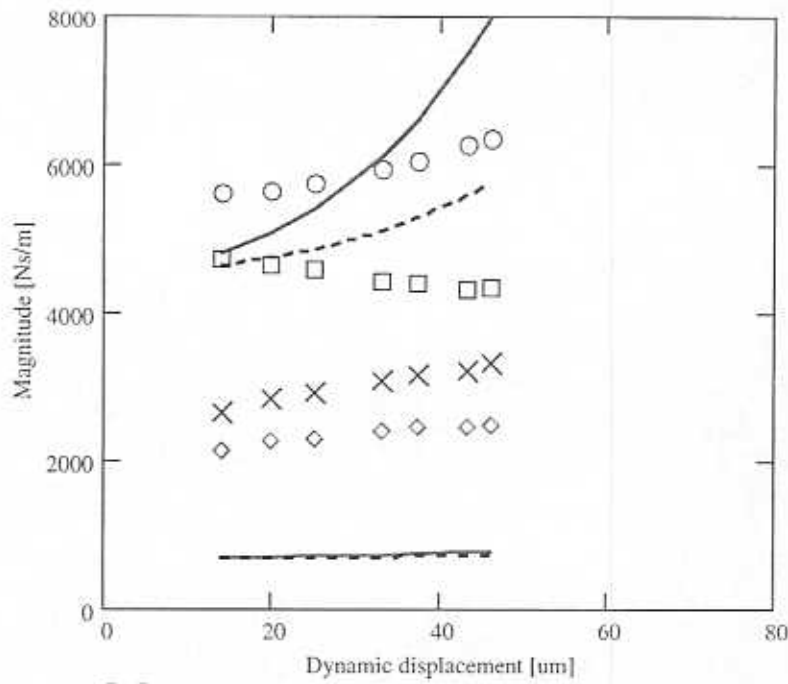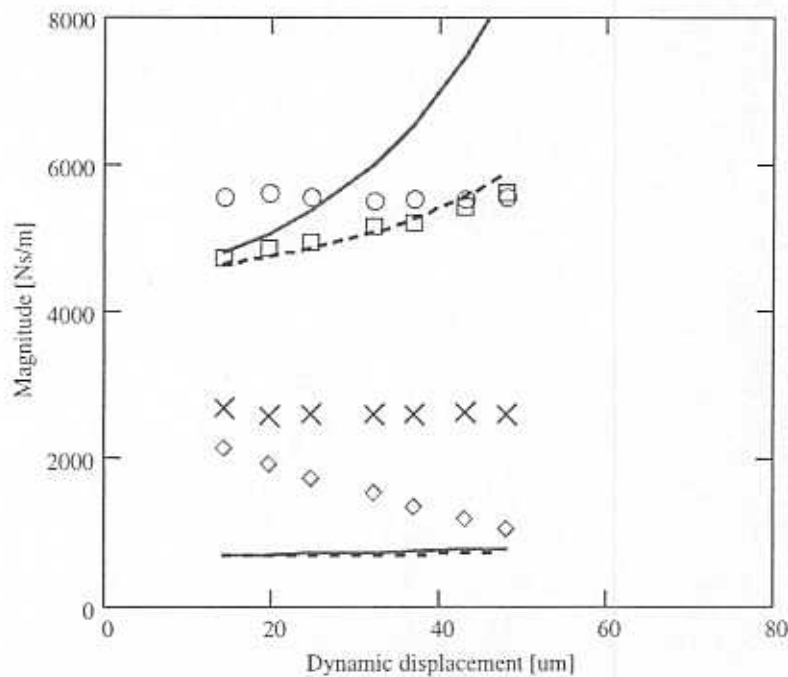
Legend:
○ ○ Cxx
□ □ Cyy
—— C-d (theory)
- - - C-c (theory)
◇   Dxx w
✕ ✕ Dyy w
—— D-d (theory)
- - - D-c (theory)

Figure 16. Test and predicted direct damping (C_{XX}, C_{YY}) and inertia (D_{XX}, D_{YY}) ω coefficients for elliptical motions; (top) $F_X > F_Y$, (bottom) $F_Y > F_X$. Test conditions: 60 Hz, 38 C, radial clearance (hot) 121 um. Predicted coefficients from short length SFD model

33
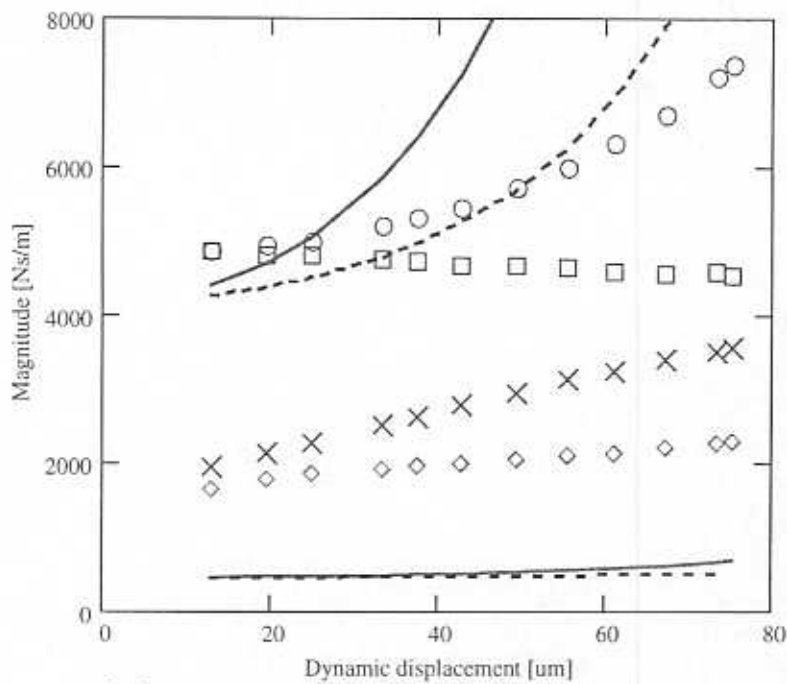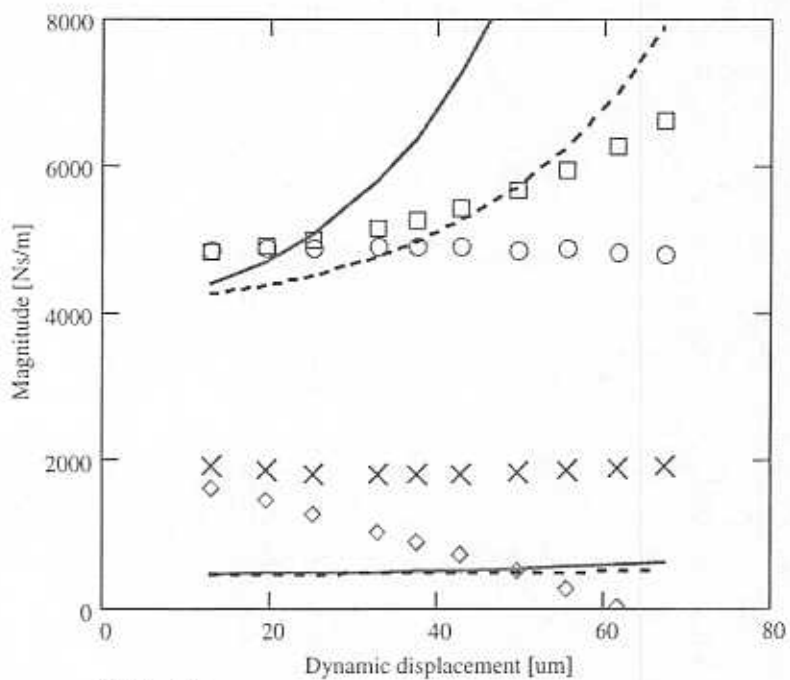
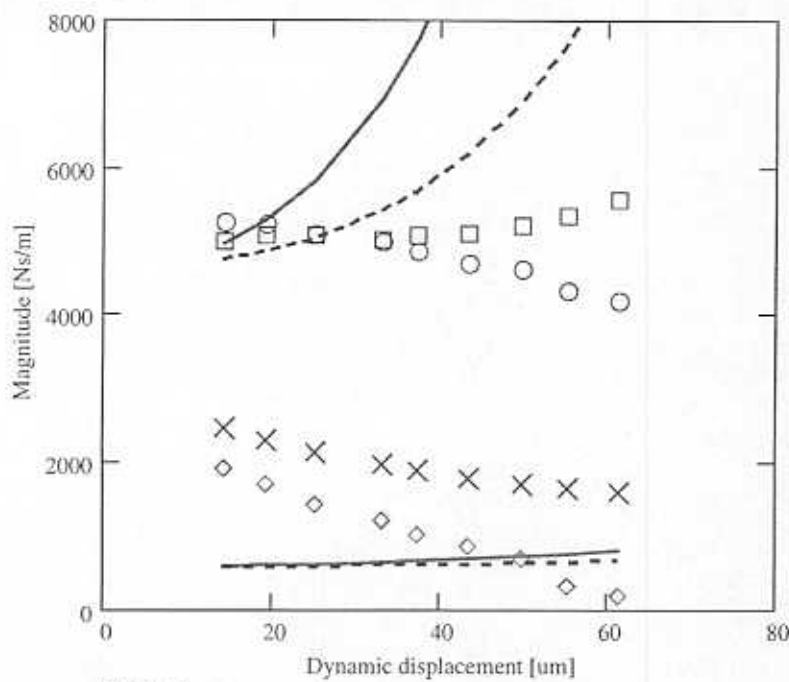**Figure 17. Test and predicted direct damping** (C_{XX}, C_{YY}) **and inertia** (D_{XX}, D_{YY}) ω **coefficients for elliptical motions; (top)** $F_X > F_Y$**, (bottom)** $F_Y > F_X$ **. Test conditions: 40 Hz, 47 C, radial clearance (hot) 114 um. Predicted coefficients from short length SFD model**
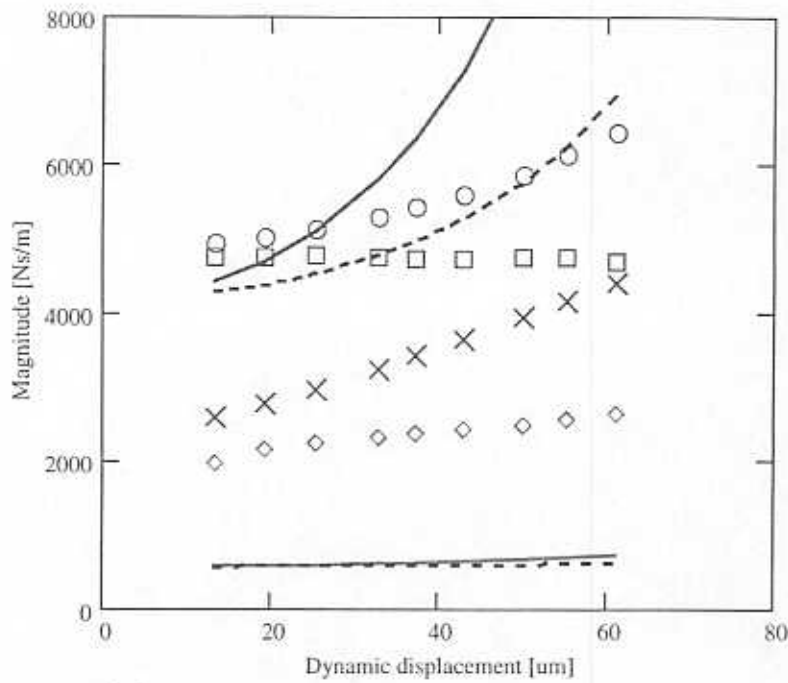
34

Fx> Fy

Lc = 0.026 [m]

ω = 50 Hz

T_h = 46.7 C

μ_h = 1.87 cP

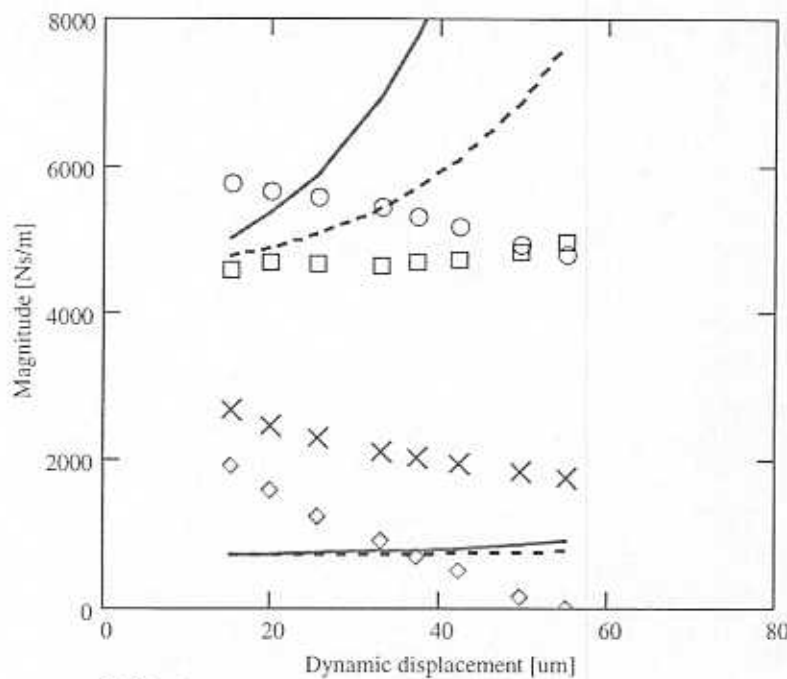C_H = 114 μm

Fy> Fx

Lc = 0.026 [m]

ω = 50 Hz

T_h = 46.7 C

μ_h = 1.87 cP

C_H = 114 μm
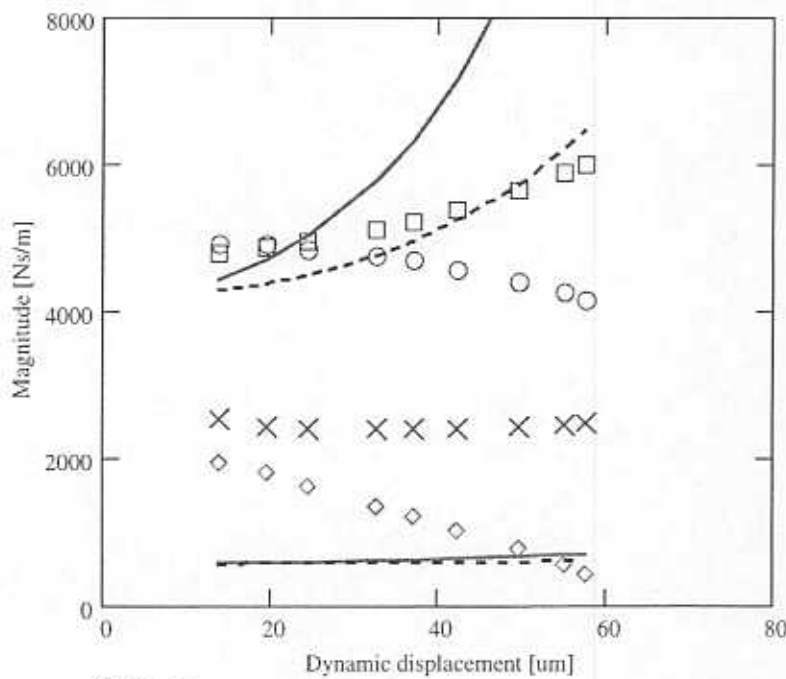
O O	Cxx
□ □	Cyy
——	C-d (theory)
- - -	C-c (theory)
◇	Dxx w
✕✕	Dyy w
——	D-d (theory)
- - -	D-c (theory)

Figure 18. Test and predicted direct damping (C_{XX}, C_{YY}) **and inertia** $(D_{XX}, D_{YY})\omega$ **coefficients for elliptical motions; (top)** $F_X > F_Y$**, (bottom)** $F_Y > F_X$ **. Test conditions: 50 Hz, 47 C, radial clearance (hot) 114 um. Predicted coefficients from short length SFD model**
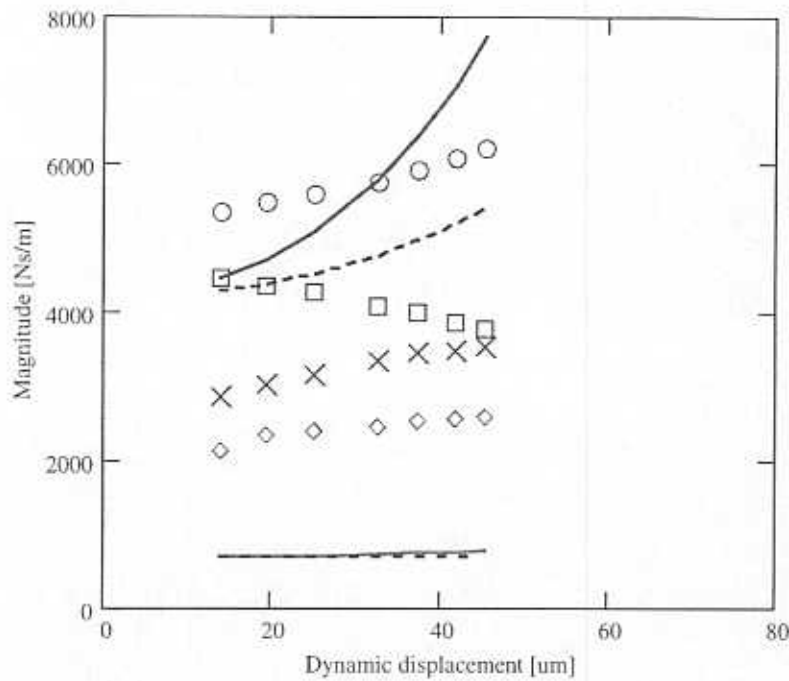
Fx> Fy

Le = 0.026 [m]

ω = 60 Hz

T_h = 46.7 C

$μ_h$ = 1.87 cP

C_H = 114 μm

Fy> Fx

Le = 0.026 [m]

ω = 60 Hz

T_h = 46.7 C

$μ_h$ = 1.87 cP

C_H = 114 μm
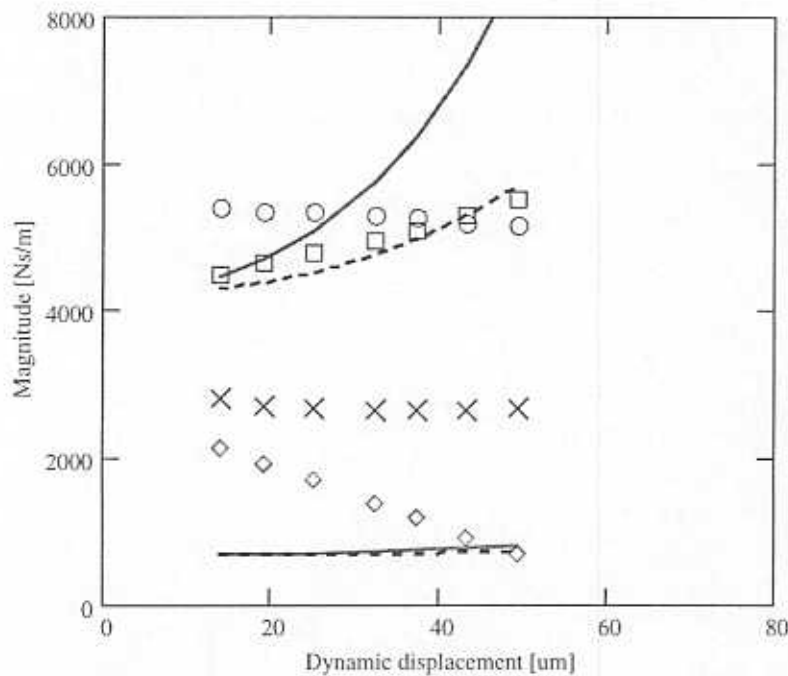
O O Cxx
□ □ Cyy
— C-d (theory)
- - - C-c (theory)
◇ Dxx w
✕ ✕ Dyy w
— D-d (theory)
- - - D-c (theory)

Figure 19 Test and predicted direct damping (C_{XX}, C_{YY}) and inertia (D_{XX}, D_{YY})ω coefficients for elliptical motions; (top) F_X> F_Y, (bottom) F_Y> F_X . Test conditions: 60 Hz, 47 C, radial clearance (hot) 114 um. Predicted coefficients from short length SFD model
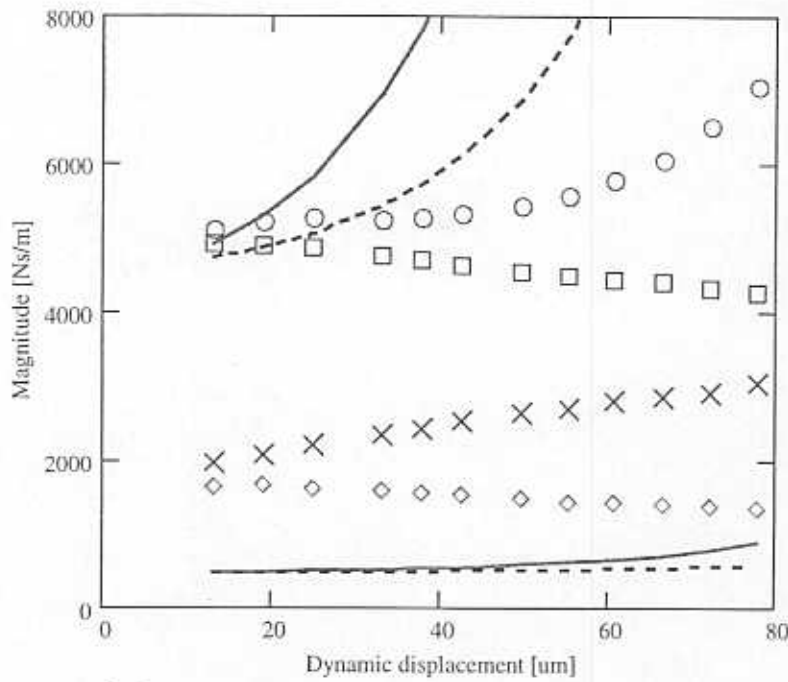
36

Figure 20. Test and predicted direct damping (C_{XX}, C_{YY}) and inertia (D_{XX}, D_{YY})ω coefficients for elliptical motions; (top) $F_X > F_Y$, (bottom) $F_Y > F_X$. Test conditions: 40 Hz, 54 C, radial clearance (hot) 102 um. Predicted coefficients from short length SFD model
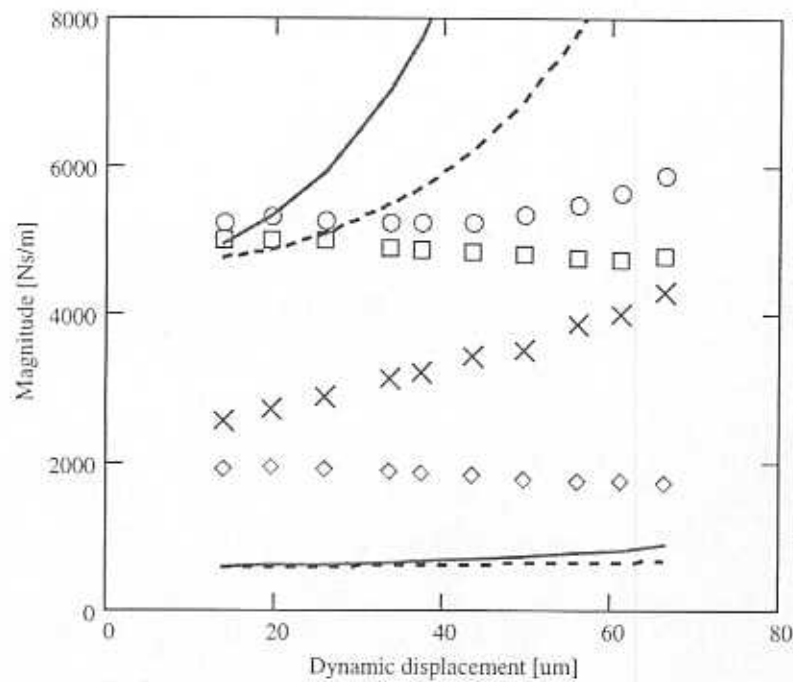
37

Fx> Fy

Le = 0.025 [m]

ω = 50 Hz

T_h = 54.4 C

μ_h = 1.59 cP

C_H = 102 μm

Fy> Fx

Le = 0.025 [m]

ω = 50 Hz

T_h = 54.4 C

μ_h = 1.59 cP

C_H = 102 μm

Figure 21. Test and predicted direct damping (C_{XX}, C_{YY}) and inertia $(D_{XX}, D_{YY})\omega$ coefficients for elliptical motions; (top) $F_X > F_Y$, (bottom) $F_Y > F_X$. Test conditions: 50 Hz, 54 C, radial clearance (hot) 102 um. Predicted coefficients from short length SFD model
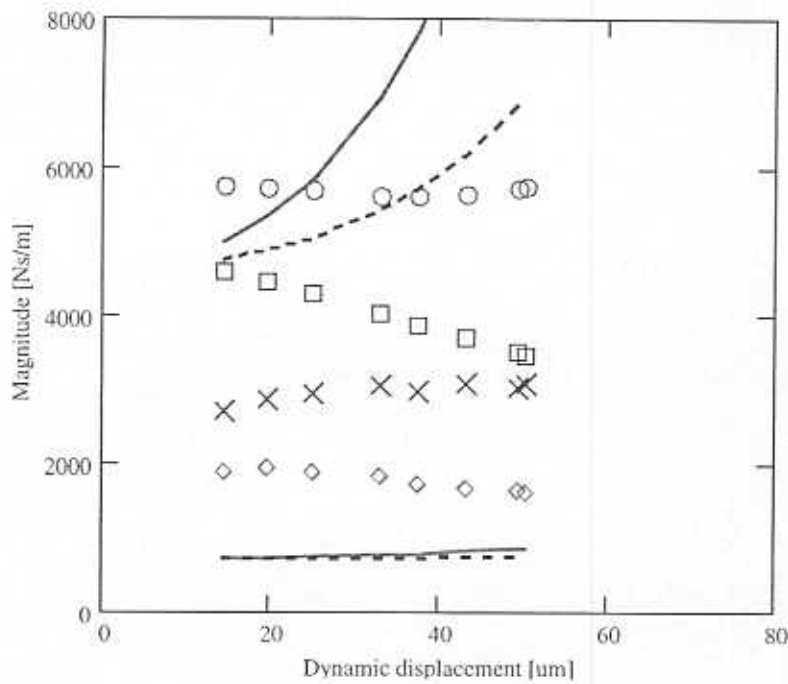
38

Fx> Fy

Lc = 0.025 [m]

ω = 60   Hz

T_h = 54.4   C

μ_h = 1.59   cP

C_H = 102   μm

Fy> Fx

Lc = 0.025 [m]

ω = 60   Hz

T_h = 54.4   C

μ_h = 1.59   cP

C_H = 102   μm

Legend:
- ○ ○ Cxx
- □ □ Cyy
- —— C-d (theory)
- - - - C-c (theory)
- ◇ Dxx w
- ✕ ✕ Dyy w
- —— D-d (theory)
- - - - D-c (theory)

Figure 22. Test and predicted direct damping (C_{XX}, C_{YY}) **and inertia** $(D_{XX}, D_{YY})\omega$
coefficients for elliptical motions; (top) $F_X > F_Y$**, (bottom)** $F_Y > F_X$ **. Test conditions: 60 Hz,**
54 C, radial clearance (hot) 102 um. Predicted coefficients from short length SFD model
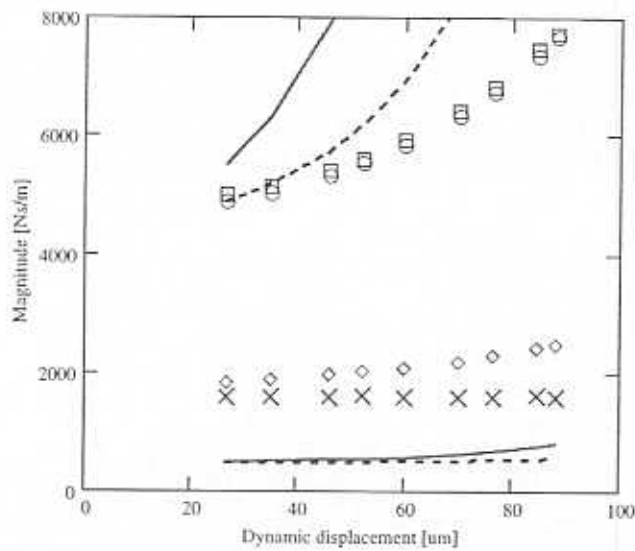
39
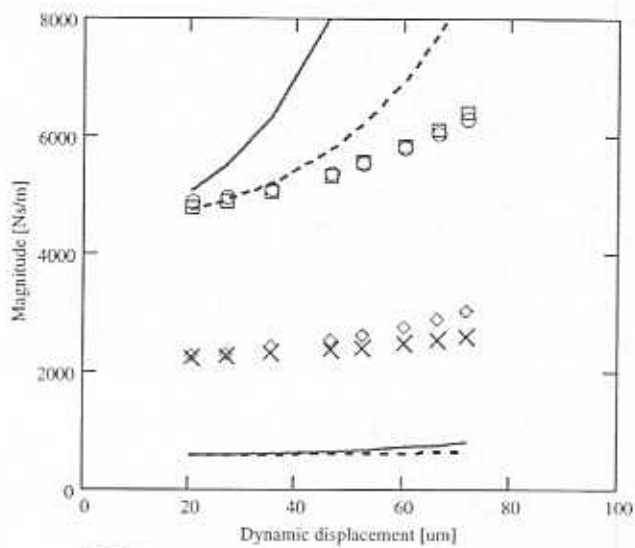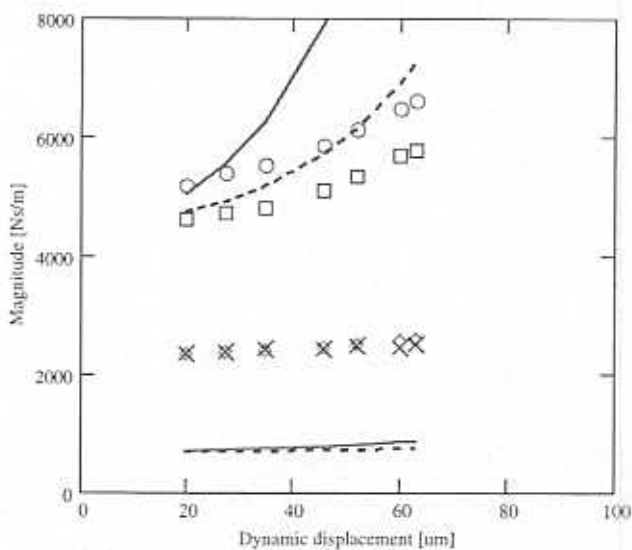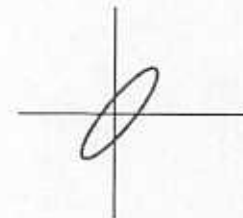
Figure 23. Test direct damping (C_{XX}, C_{YY}) and inertia $(D_{XX}, D_{YY})\omega$ coefficients for elliptical motions; $F_X = F_Y$. Test conditions: 40, 50, 60 Hz, 38 C, radial clearance (hot) 121 um. Predicted coefficients from short length SFD model.
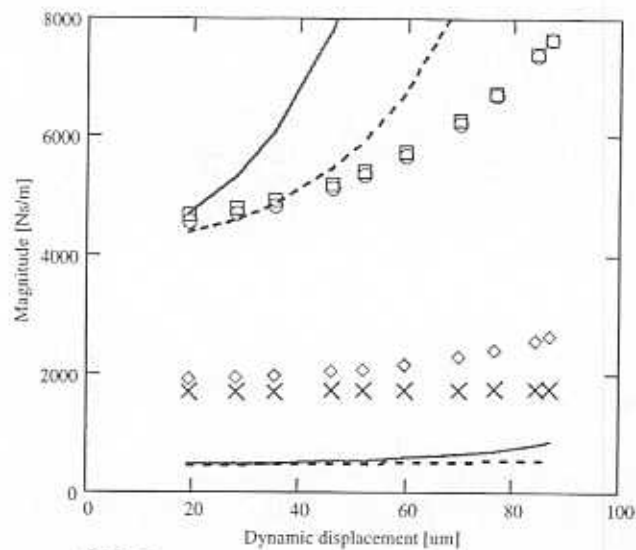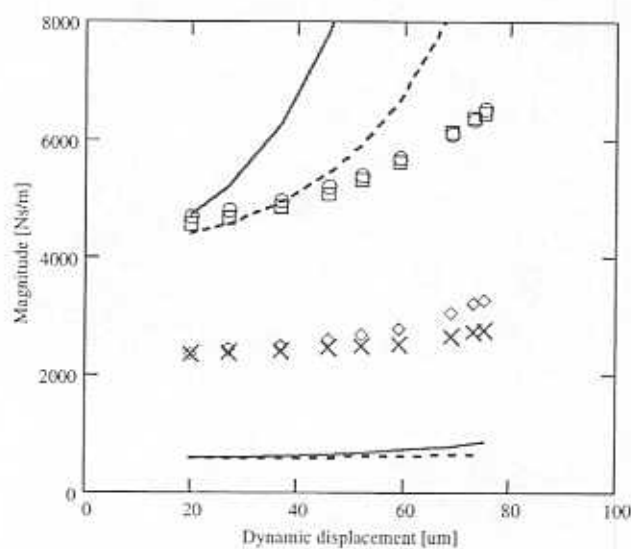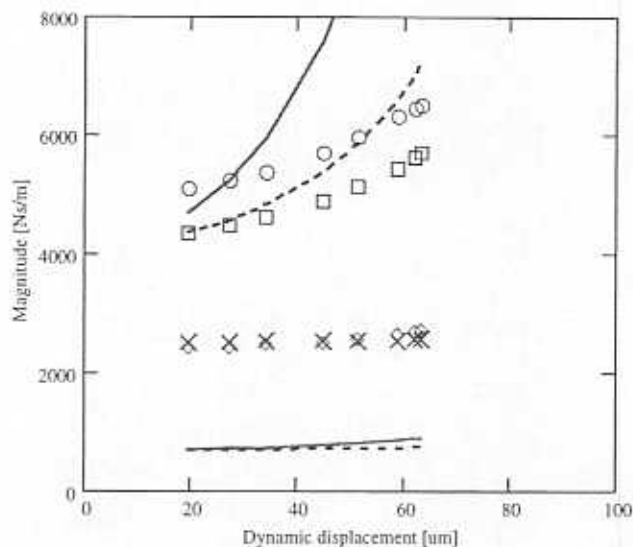
Figure 24. Test direct damping (C_{XX}, C_{YY}) and inertia $(D_{XX}, D_{YY})\omega$ coefficients for elliptical motions; $F_X = F_Y$. Test conditions: 40, 50, 60 Hz, 47 C, radial clearance (hot) 114 um

41
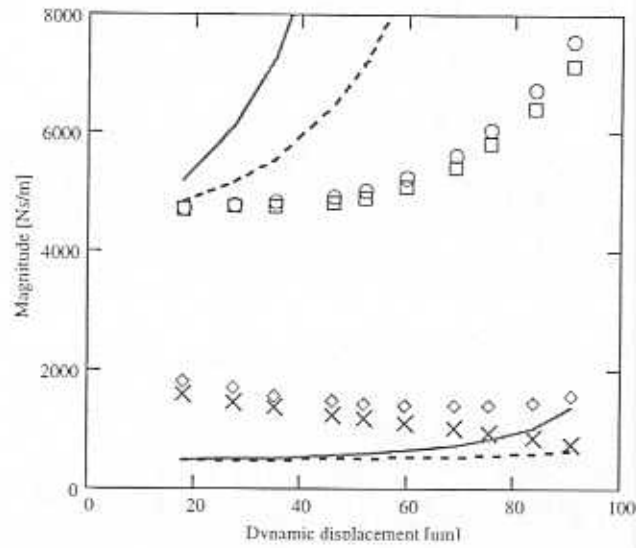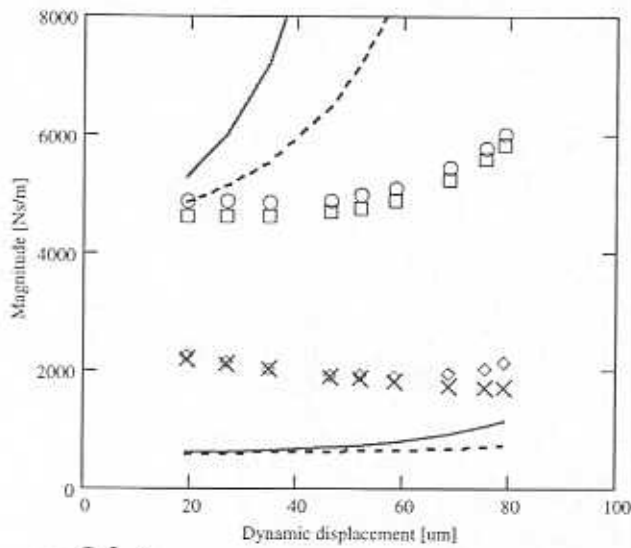
Figure 25. Test direct damping (C_{XX}, C_{YY}) and inertia (D_{XX}, D_{YY}) ω coefficients for elliptical motions; $F_X = F_Y$. Test conditions: 40, 50, 60 Hz, 54.4 C, radial clearance (hot) 102 um
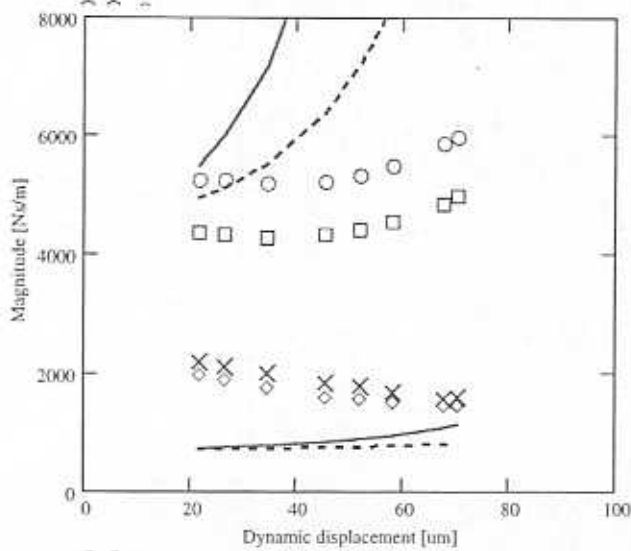
42

$\omega = 40$ Hz $T_h = 54.4$ C $\mu_h = 1.59$ cP $C_H = 102$ μm

Elliptical motions 45 deg

$FX_{nn} = 13.936$ [N]

$FY_{nn} = 16.518$

$a_{nn} = 17.678$ [um]

$b_{nn} = 2.874$

— Top PT
···· Bottom PT

Elliptical motions 45 deg

$FX_{nn} = 51.922$ [N]

$FY_{nn} = 58.106$

$a_{nn} = 59.467$ [um]

$b_{nn} = 9.655$

— Top PT
···· Bottom PT

Elliptical motions 45 deg

$FX_{nn} = 114.491$ [N]

$FY_{nn} = 122.855$

$a_{nn} = 90.676$ [um]

$b_{nn} = 16.871$

— Top PT
···· Bottom PT

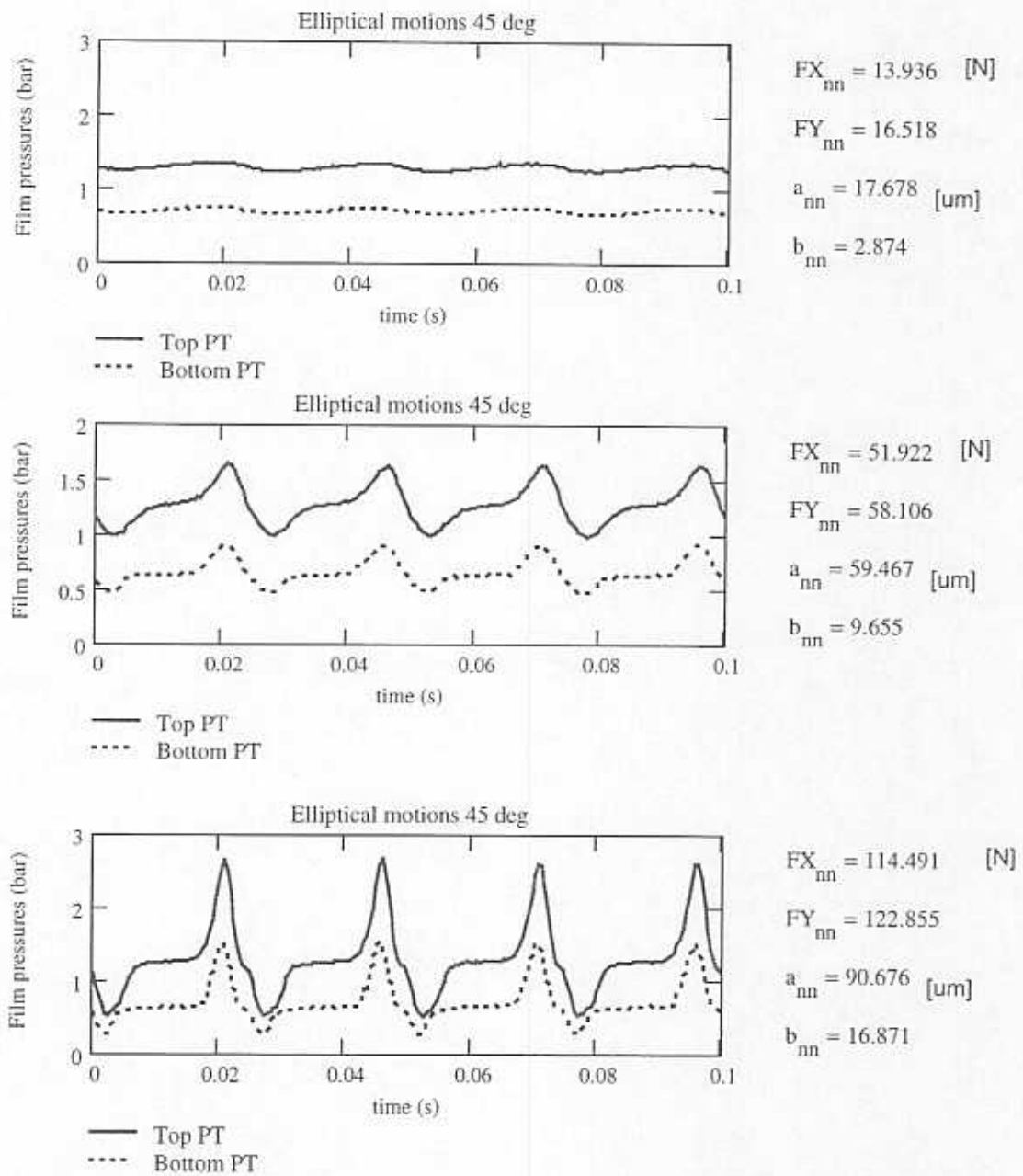**Figure 26. Dynamic squeeze film pressures versus time for elliptical motions (45 ° oriented). Test conditions: 40 Hz, 54 °C. Peak forces (x,y) and ellipse amplitudes (a,b) noted. (Top) lowest amplitude, (Middle) moderate amplitude, (Bottom) largest amplitude.**

$\omega = 60$ Hz $\quad T_h = 54.4$ C $\quad \mu_h = 1.59$ cP $\quad C_H = 102$ µm

Elliptical motions 45 deg

$FX_{nn} = 34.224$ [N]

$FY_{nn} = 30.415$

$a_{nn} = 21.428$ [um]

$b_{nn} = 2.754$

—— Top PT
···· Bottom PT

Elliptical motions 45 deg

$FX_{nn} = 81.638$ [N]

$FY_{nn} = 71.26$

$a_{nn} = 51.887$ [um]

$b_{nn} = 6.341$

—— Top PT
···· Bottom PT

Elliptical motions 45 deg

$FX_{nn} = 121.593$ [N]

$FY_{nn} = 105.104$

$a_{nn} = 70.311$ [um]

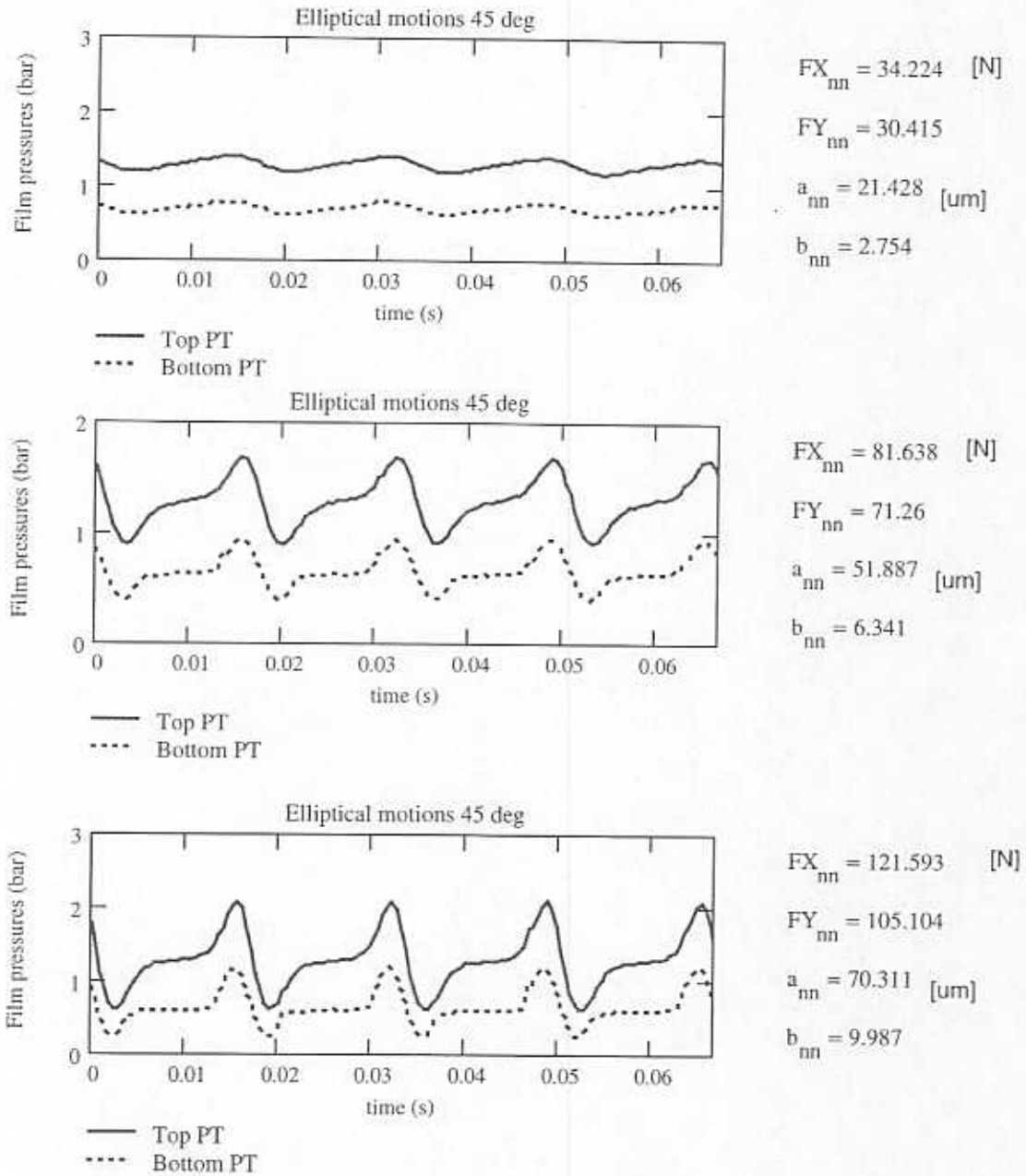$b_{nn} = 9.987$

—— Top PT
···· Bottom PT

Figure 27. Dynamic squeeze film pressures versus time for elliptical motions (45 ° oriented). Test conditions: 60 Hz, 54 °C. Peak forces (x,y) and ellipse amplitudes (a,b) noted. (Top) lowest amplitude, (Middle) moderate amplitude, (Bottom) largest amplitude.
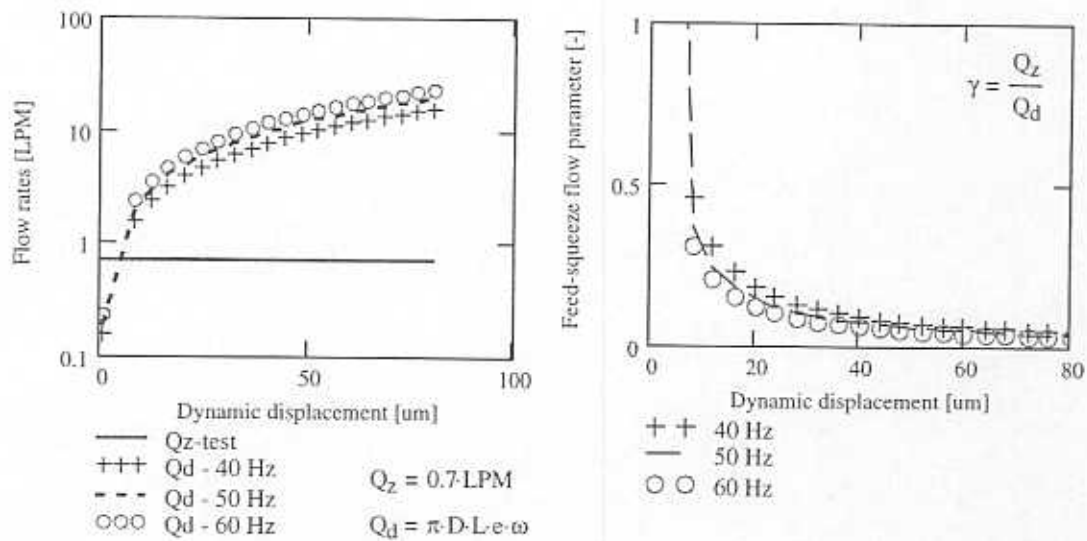
44

Figure 28. (a) Axial flow rate and dynamic film volume change (Q_d) versus amplitude of motion, (b) Feed-squeeze flow parameter (γ) versus amplitude of motion for increasing whirl frequencies.
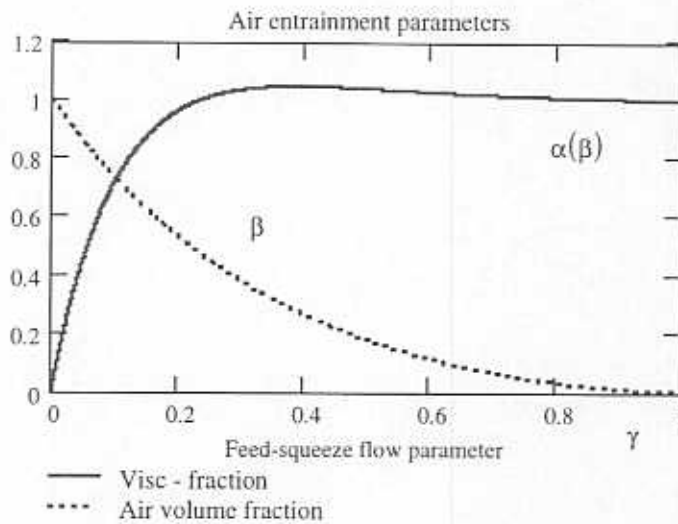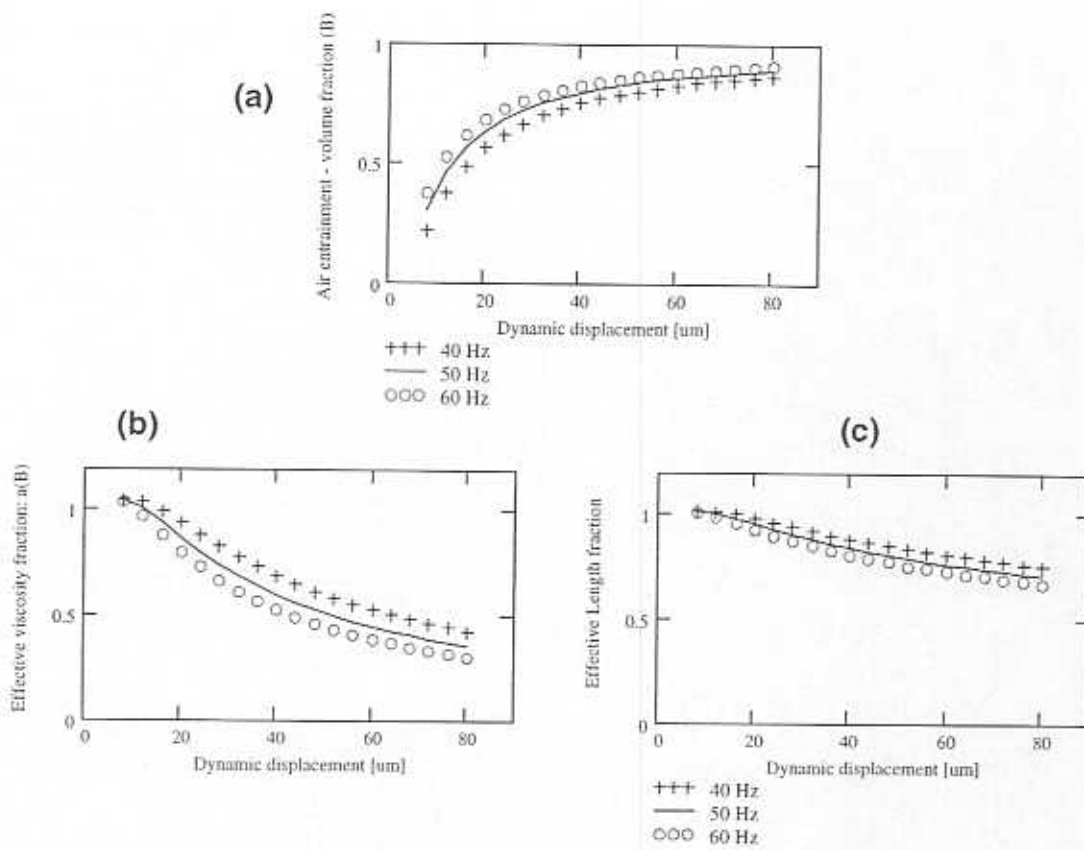

Figure 29. Air in oil volume fraction (β) and effective viscosity fraction $\alpha(\beta)$ versus feed/squeeze flow parameter (γ). Severity of air entrainment decreases as $\gamma \rightarrow 1$.

Figure 30. Predicted air entrainment volume fraction (β) and effective viscosity fraction $\alpha(\beta)$ OR effective length fraction $l_{(\beta)}$ versus the amplitude of dynamic motion for test frequencies: 40, 50 and 60 Hz.